Finite Elements in Analysis and Design 164 (2019) 18–41

Contents lists available at ScienceDirect

Finite Elements in Analysis and Design

journal homepage: www.elsevier.com/locate/finel

Bi-material topology optimization for energy dissipation with inertia and material rate effects under finite deformations

Ryan Alberdi [a], Kapil Khandelwal [b,*]

[a] Graduate Student, Dept. of Civil & Env. Engg. & Earth Sci., University of Notre Dame, United States
[b] Associate Professor, Dept. of Civil & Env. Engg. & Earth Sci., 156 Fitzpatrick Hall, University of Notre Dame, Notre Dame, IN, 46556, United States

ARTICLE INFO

Keywords:
Nonlinear topology optimization
Finite deformation viscoplasticity
Transient dynamic analysis
Bi-material design
Adjoint sensitivity analysis

ABSTRACT

In this study, a bi-material topology optimization framework is developed for maximizing plastic energy dissipation under a combination of material rate effects, inertia effects, and large deformations. In the developed framework, rate effects are considered by employing a finite deformation viscoplastic model and finite element analysis is carried out using F-bar elements for spatial discretization and the Hilber-Hughes-Taylor algorithm for time integration. A bi-material interpolation strategy is proposed within the density-based design parameterization and used to combine material phases with different phenomenological behavior. Consistent design sensitivities are obtained using a time-dependent adjoint method. Design examples reveal that a much higher percentage of the total energy can be dissipated as plastic work when a soft energy dissipating elasto-viscoplastic phase is combined in an optimized way with a stiffness providing hyperelastic phase than when the energy dissipating phase is considered alone. Moreover, isolating the influence of material rate effects from inertia effects provides insight into how optimized designs can exploit these phenomena.

1. Introduction

Since the seminal paper by Bendsøe and Kikuchi [1], topology optimization has developed into one of the most successful computational design tools employed in the field of mechanics, with approaches formulated for a variety of design problems, see e.g. the reviews in Refs. [2–5]. In many cases, topology optimization approaches have matured to the point where they are included in commercial software packages regularly used by engineers in practice [6,7]. Much of this progress has been directed toward design objectives such as stiffness or related variants (natural frequency, etc.). However, for design applications involving a large amount of energy entering a system in a short span of time, effort is often focused on designing protective structures for the objective of energy dissipation. The need for energy dissipating protective structures permeates a number of engineering disciplines such as structural, aerospace, automotive, and sports engineering, where impact mitigation is an important design criterion. For instance, energy dissipating devices and structures are used as impact resistant exteriors for spacecraft, buffers in vehicles, sacrificial cladding in building systems, and protective layers in personal safety equipment, among others [8]. Energy dissipation is achieved by arranging materials to exploit irreversible phenomena such as plasticity, as is the case with the majority of structures and structural components made from metals and polymers.

While it is a growing research area, there are at present only a handful of studies that consider plasticity in topology optimization. Early works have employed elastoplastic material models within topology optimization formulations aimed at maximizing ductility in the form of internal work [9–12], or maximizing structural stiffness in steel reinforced concrete structures [13]. Additionally, several recent studies have considered the objective of maximizing plastic energy dissipation using different elastoplastic material models [14–16] and coupled elastoplastic-damage models [17,18]. The types of impact mitigation applications where improved energy dissipation is desired, however, often involve structures subject to both large deformations and rapid loading rates, which cannot be accounted for within the rate-independent small strain formulations employed in the preceding studies. Finite deformation elastoplastic models can account for large deformations, and one such model was employed in Ref. [19] to carry out topology optimization for plastic energy dissipation. On the other hand, material rate effects – e.g. the need for higher stresses to induce plastic flow – may become prominent under rapid application of loading, and can be simulated using viscoplastic material models wherein plastic flow is rate dependent. Development of topology optimization approaches which account for these phenomena remains an open research area.

* Corresponding author.
E-mail address: kapil.khandelwal@nd.edu (K. Khandelwal).

https://doi.org/10.1016/j.finel.2019.06.003
Received 14 December 2018; Received in revised form 3 April 2019; Accepted 7 June 2019
Available online 27 June 2019

Under the rapid application of loading which can cause material rate effects to become prominent, inertia effects also cannot be ignored. These inertia effects can significantly affect how energy dissipation takes place in structures, and require dynamic analyses taking place in the time domain. The existing literature is scant regarding use of such dynamic analyses within topology optimization. Transient dynamic analysis was considered in Ref. [20] to account for the influence of inertia effects, but restricted to small strain elasticity. Transient analysis for energy dissipation using viscoelasticity has been considered in Refs. [21,22], but design scenarios consider longer time periods and harmonic loading instead of the short impulse loading present in impact mitigation applications where plastic energy dissipation is desired. In the study by Nakshatrala and Tortorelli [23], a transient formulation making use of a rate-independent plasticity model was employed to minimize the strain energy at a given point in a design domain. This formulation used a bi-material interpolation scheme to control energy propagation in the form of a shock wave resulting from impulse loading, but again was developed in the small strain regime and without accounting for material rate effects. More recently, the study by Ivarsson et al. [24] accounts for the relevant phenomena by employing a finite deformation viscoplastic model along with transient dynamic analysis. The focus is on maximizing the plastic work within a design domain subject to different applied rates of loading, ranging from the quasi-static limit to high rates. While influence of this loading rate on the evolution of optimized topologies was investigated, it is unclear whether certain topological features resulted from the phenomena of rate dependent plastic flow or are to be attributed to inertia effects, as these phenomena are not isolated.

In this study, a topology optimization formulation is developed for maximizing energy dissipation while considering the phenomena of material rate effects, inertia effects, and large deformations. The finite deformation dynamic equations of motion are spatially discretized using F-bar finite elements [25] to account for incompressibility constraints and the resulting semi-discrete initial value problem is integrated in time using the Hilber-Hughes-Taylor (HHT) algorithm [26]. Material rate effects are considered by employing a viscoplastic model developed in the finite deformation regime and numerically implemented using the exponential return mapping algorithm. Designs are parameterized using the density-based approach and a bi-material interpolation strategy is developed to combine material phases with entirely separate phenomenological behavior. To compute sensitivity values, the general path-dependent adjoint formulation developed in Ref. [27] – which readily accommodates the numerical procedures employed to carry out finite deformation dynamic elastoplastic analysis – is followed. Design examples reveal that energy dissipation can be increased when a soft energy dissipating elasto-viscoplastic material phase is combined with a hard hyperelastic phase providing stiffness, rather than used alone. These examples also consider inertia and material rate effects in isolation and in combination so that their influence on optimized topologies can be discussed.

The study is organized as follows: Section 2 introduces the governing dynamic equations of motion for deformable bodies undergoing finite deformations and their numerical implementation, including the F-bar finite element formulation and HHT time integration algorithm. Constitutive models used for both material phases are also introduced in this section. Section 3 then presents the topology optimization approach used, including the developed bi-material interpolation scheme and specification of the general adjoint sensitivity analysis. Numerical examples demonstrating the capability of the developed framework are covered in Section 4 and then Section 5 offers concluding remarks.

2. Dynamic finite element analysis

In this section, the dynamic equations of motion for deformable bodies undergoing finite deformations are laid out in Lagrangian form. Numerical discretization in both space and time is covered, with F-bar finite elements used in spatial discretization and the Hilber-Hughes-Taylor algorithm employed for time integration. The constitutive relations governing material behavior of the different phases is also presented.

2.1. Equations of motion

The dynamic equations of motion presented herein are formulated in a Lagrangian approach, where the Lagrangian displacement field $\boldsymbol{u}(\boldsymbol{X}) = \boldsymbol{\varphi}(\boldsymbol{X}) - \boldsymbol{X}$ and corresponding Lagrangian velocity and acceleration fields $\dot{\boldsymbol{u}}(\boldsymbol{X},t) = \dot{\boldsymbol{\phi}}(\boldsymbol{X},t)$ and $\ddot{\boldsymbol{u}}(\boldsymbol{X},t) = \ddot{\boldsymbol{\phi}}(\boldsymbol{X},t)$ are defined in terms of the deformation $\boldsymbol{\phi} : \Omega_0 \rightarrow \Omega_t$ which maps the reference configuration Ω_0 to the current configuration Ω_t. The boundary $\partial\Omega_0$ of the reference configuration is considered to be split into the disjoint sets $\partial\Omega_{0u}$ and $\partial\Omega_{0\sigma}$ such that $\partial\Omega_0 = \partial\Omega_{0u} \cup \partial\Omega_{0\sigma}$ and $\partial\Omega_{0u} \cap \partial\Omega_{0\sigma} = \varnothing$. Dirichlet boundary conditions in the form of displacements are applied to $\partial\Omega_{0u}$ while Neumann boundary conditions in the form of surface tractions are applied to $\partial\Omega_{0\sigma}$. Motion is then governed by the following Lagrangian initial boundary value problem.

$$
\begin{aligned}
&\text{Given } \boldsymbol{b}_0(\boldsymbol{X},t) : \Omega_0 \times \mathbb{R} \rightarrow \mathbb{R}^3, \boldsymbol{u}^p(\boldsymbol{X},t) : \partial\Omega_{0u} \times \mathbb{R} \rightarrow \mathbb{R}^3, \boldsymbol{T}^p(\boldsymbol{X},t) : \partial\Omega_{0\sigma} \times \mathbb{R} \rightarrow \mathbb{R}^3 \\
&\text{Find } \boldsymbol{u}(\boldsymbol{X},t) : \overline{\Omega}_0 \times \mathbb{R} \rightarrow \mathbb{R}^3 \text{ such that} \\
&\nabla.\boldsymbol{P} + \boldsymbol{b}_0 = \rho_0 \ddot{\boldsymbol{u}} \qquad \text{in } \Omega_0 \\
&\boldsymbol{u} = \boldsymbol{u}^p(\boldsymbol{X},t) \quad \text{on } \partial\Omega_{0u} \\
&\boldsymbol{T} = \boldsymbol{P}.\boldsymbol{N} = \boldsymbol{T}^p(\boldsymbol{X},t) \quad \text{on } \partial\Omega_{0\sigma} \\
&\boldsymbol{u}(\boldsymbol{X},t)|_{t=0} = \boldsymbol{u}_0(\boldsymbol{X}) \\
&\dot{\boldsymbol{u}}(\boldsymbol{X},t)|_{t=0} = \dot{\boldsymbol{u}}_0(\boldsymbol{X})
\end{aligned} \tag{1}
$$

where $\overline{\Omega}_0 = \Omega_0 \cup \partial\Omega_0$ is the closure of Ω_0, ρ_0 is the mass density per unit reference volume, $\boldsymbol{b}_0$ is the body force per unit reference volume, and $\boldsymbol{u}^p$ and $\boldsymbol{T}^p$ are the prescribed boundary displacement and traction values. The initial conditions $(1)_4$ and $(1)_5$ supplement the second order (in time) partial differential equation $(1)_1$.

Constructing the weak form of Eq. (1) and applying the standard Galerkin procedure results in the following semidiscrete equation of motion

$$
\boldsymbol{F}_{int}(\boldsymbol{u}) - \boldsymbol{F}_{ext} + \boldsymbol{M}\ddot{\boldsymbol{u}} = 0 \tag{2}
$$

with

$$
\boldsymbol{F}_{int} = \mathop{\mathscr{A}}_{e=1}^{n_{ele}} \boldsymbol{F}^e_{int} \text{ and } \boldsymbol{F}_{ext} = \mathop{\mathscr{A}}_{e=1}^{n_{ele}} \boldsymbol{F}^e_{ext} \; \boldsymbol{M} = \mathop{\mathscr{A}}_{e=1}^{n_{ele}} \boldsymbol{M}_e \tag{3}
$$

where $\boldsymbol{u}$ and $\ddot{\boldsymbol{u}}$ are the nodal displacement and acceleration values, respectively, $\mathscr{A}$ denotes the finite element assembly operator, and n_{ele} is the total number of finite elements in the domain. In order to account for incompressibility constraints such as those imposed by pressure independent plastic flow, the F-bar finite element formulation is utilized [28]. Within a given element$e$, the deformation gradient $\boldsymbol{F} = \partial\boldsymbol{\phi}/\partial\boldsymbol{X}$ is computed in discrete form using the element shape function derivative matrix $\boldsymbol{B}_e$ and element displacement vector $\boldsymbol{u}_e$ as $\boldsymbol{F} = \boldsymbol{B}_e\boldsymbol{u}_e + \boldsymbol{I}$. In standard displacement-based finite element formulations, the deformation gradient is used directly in constitutive algorithms. In the F-bar formulation, however, constitutive algorithms are evaluated using a quantity $\overline{\boldsymbol{F}}$ which provides constant pressure throughout the element [28] and is defined as

$$
\bar{\boldsymbol{F}} = r^a \boldsymbol{F} \qquad r = \frac{\det \boldsymbol{F}_0}{\det \boldsymbol{F}} \tag{4}
$$

Here $\boldsymbol{F}_0 = \boldsymbol{B}^0_e\boldsymbol{u}_e + \boldsymbol{I}$, $\boldsymbol{B}^0_e$ is the shape function derivative matrix evaluated at the element centroid and the exponent a is 1/2 for two dimensional problems and 1/3 for three dimensional problems. The element external force vector and $\boldsymbol{F}^e_{ext}$ and mass matrix $\boldsymbol{M}_e$ are not affected by the

F-bar formulation, and are given as

$$\boldsymbol{F}^e_{ext}(t) = \int_{\Omega^e_0} \boldsymbol{N}^T_e \boldsymbol{b}_0 dV + \int_{\partial\Omega^e_{0\sigma}} \boldsymbol{N}^T_e \boldsymbol{T}^p dS \quad \boldsymbol{M}^e = \int_{\Omega^e_0} \rho_0 \boldsymbol{N}^T_e \boldsymbol{N}_e dV \tag{5}$$

where Ω^e_0 is the reference domain of element e and $\boldsymbol{N}_e$ is the element shape function matrix in the reference configuration. Using $\overline{\boldsymbol{F}}$ in the constitutive algorithm returns the stress tensor $\overline{\boldsymbol{P}}(\overline{\boldsymbol{F}})$, but the element internal force vector $\boldsymbol{F}^e_{int}$ is defined in terms of the first Piola-Kirchhoff stress tensor $\boldsymbol{P}(\boldsymbol{F})$. Hence, for the F-bar formulation, $\boldsymbol{F}^e_{int}$ is

$$\boldsymbol{F}^e_{int} = \boldsymbol{F}^e_{int}(\boldsymbol{u}_e, t) = \int_{\Omega^e_0} r^{a-1} \boldsymbol{B}^T_e \overline{\boldsymbol{P}} dV \tag{6}$$

where use is made of the relation $\boldsymbol{P} = r^{a-1}\overline{\boldsymbol{P}}$. The tangent stiffness matrix needed for global Newton-Raphson iterations is also altered by the F-bar formulation, and is obtained by linearizing Eq. (6) as

$$\begin{aligned} \boldsymbol{K}_T &= \overset{n_{ele}}{\mathscr{A}}_{e=1} \boldsymbol{K}^e_T \\ \boldsymbol{K}^e_T &= \int_{\Omega^e_0} \boldsymbol{B}^T_e \left[\overline{\mathbb{A}}_T - a\overline{\mathbb{A}}_T : \left(\overline{\boldsymbol{F}} \otimes \overline{\boldsymbol{F}}^{-T}\right) + a\overline{\boldsymbol{P}} \otimes \overline{\boldsymbol{F}}^{-T}\right] \boldsymbol{B}_e dV \\ &\quad + \int_{\Omega^e_0} \boldsymbol{B}^T_e \left[ar^{a-1}\overline{\mathbb{A}}_T : \overline{\boldsymbol{F}} \otimes \boldsymbol{F}^{-T}_0 - ar^{a-1}\overline{\boldsymbol{P}} \otimes \boldsymbol{F}^{-T}_0\right] \boldsymbol{B}^0_e dV \end{aligned} \tag{7}$$

where $\overline{\mathbb{A}}_T$ is the algorithmic consistent tangent returned from the constitutive algorithm. The semidiscrete equation of motion Eq. (2) – combined with initial conditions $\boldsymbol{u}|_{t=0} = \boldsymbol{u}_0$ and $\dot{\boldsymbol{u}}|_{t=0} = \dot{\boldsymbol{u}}_0$ – forms an initial value problem that fully determines the motion of a body at a given time and requires a time integration scheme to solve.

Integration is carried out using the Hilber, Highes and Taylor method [26] which allows for the use of numerical damping to filter out unwanted high frequency components. This method approximates the initial value problem as

$$\begin{aligned} &(1+\alpha)\boldsymbol{F}_{int}(\boldsymbol{u}_{k+1}) - \alpha\boldsymbol{F}_{int}(\boldsymbol{u}_k) - \boldsymbol{F}_{ext}(t_{k+1}) + \boldsymbol{M}\boldsymbol{a}_{k+1} = \boldsymbol{0} \\ &\boldsymbol{u}_{k+1} = \boldsymbol{u}_k + \Delta t \boldsymbol{v}_k + \frac{\Delta t^2}{2}(1-2\beta)\boldsymbol{a}_k + \beta\Delta t^2 \boldsymbol{a}_{k+1} \\ &\boldsymbol{v}_{k+1} = \boldsymbol{v}_k + (1-\gamma)\Delta t \boldsymbol{a}_k + \gamma\Delta t \boldsymbol{a}_{k+1} \end{aligned} \tag{8}$$

where $\Delta t = t_{k+1} - t_k$ is the time step and α, γ, and β are parameters that determine the amount of numerical damping, accuracy, and stability of the algorithm, respectively. The standard Newmark method can be recovered by setting $\alpha = 0$. Equation (8) forms a set of algebraic equations for the unknown displacement, velocity and acceleration vectors $\boldsymbol{u}_{k+1}$, $\boldsymbol{v}_{k+1}$ and $\boldsymbol{a}_{k+1}$, respectively. There are a number of ways to solve this system, but the u-form is employed in this study, resulting in one nonlinear equation in terms of the unknown $\boldsymbol{u}_{k+1}$

$$\begin{aligned} \boldsymbol{R}(\boldsymbol{u}_{k+1}) &= (1+\alpha)\boldsymbol{F}_{int}(\boldsymbol{u}_{k+1}) - \alpha\boldsymbol{F}_{int}(\boldsymbol{u}_k) - \boldsymbol{F}_{ext}(t_{k+1}) + \frac{1}{\beta\Delta t^2}\boldsymbol{M}(\boldsymbol{u}_{k+1} - \tilde{\boldsymbol{u}}_{k+1}) \\ &= \boldsymbol{0} \end{aligned} \tag{9}$$

This equation is solved using the Newton-Raphson method with tangent

$$\frac{d\boldsymbol{R}(\boldsymbol{u}_{k+1})}{d\boldsymbol{u}_{k+1}} = (1+\alpha)\boldsymbol{K}_T + \frac{1}{\beta\Delta t^2}\boldsymbol{M} \tag{10}$$

where $\boldsymbol{K}_T$ is the tangent stiffness matrix given in Eq. (7). Once $\boldsymbol{u}_{k+1}$ is known it is used to update the other unknowns as

$$\begin{aligned} \boldsymbol{a}_{k+1} &= \frac{1}{\beta\Delta t^2}(\boldsymbol{u}_{k+1} - \tilde{\boldsymbol{u}}_{k+1}) \\ \boldsymbol{v}_{k+1} &= \tilde{\boldsymbol{v}}_{k+1} + \frac{\gamma}{\beta\Delta t}(\boldsymbol{u}_{k+1} - \tilde{\boldsymbol{u}}_{k+1}) \end{aligned} \tag{11}$$

Predictors $\tilde{\boldsymbol{u}}_{k+1}$ and $\tilde{\boldsymbol{v}}_{k+1}$ are defined in terms of the previous step values as

$$\begin{aligned} \tilde{\boldsymbol{u}}_{k+1} &= \boldsymbol{u}_k + \Delta t \boldsymbol{v}_k + \frac{\Delta t^2}{2}(1-2\beta)\boldsymbol{a}_k \\ \tilde{\boldsymbol{v}}_{k+1} &= \boldsymbol{v}_k + (1-\gamma)\Delta t \boldsymbol{a}_k \end{aligned} \tag{12}$$

More information on this algorithm can be found in Ref. [26].

2.2. Constitutive models

In this study, different constitutive models are used to represent the two material phases combined during topology optimization. The first is a hyperelastic model with free energy ψ considered to be split into isochoric ψ_{iso} and volumetric ψ_{vol} parts. The isochoric function is chosen as the regularized Ogden model, defined in terms of the principal stretches $\lambda_a, a = 1, 2, 3$ (i.e. the eigenvalues of the right Cauchy-Green tensor $\boldsymbol{C} = \boldsymbol{F}^T.\boldsymbol{F}$) as

$$\begin{aligned} \psi_{iso}(\lambda_1, \lambda_2, \lambda_3) &= \sum_{p=1}^{N_{mt}} \frac{G_p}{\alpha_p}\left[\overline{\lambda}_1^{\alpha_p} + \overline{\lambda}_2^{\alpha_p} + \overline{\lambda}_3^{\alpha_p} - 3\right] \\ \overline{\lambda}_a &= J^{-1/3}\lambda_a = \frac{\lambda_a}{(\lambda_1\lambda_2\lambda_3)^{1/3}} = \lambda_a^{\frac{2}{3}}(\lambda_b\lambda_c)^{-\frac{1}{3}} \end{aligned} \tag{13}$$

where $J = \det\boldsymbol{F}$ is the volumetric Jacobian, N_{mt} is the number of terms considered in the strain energy function, G_p are constant shear moduli, and α_p are dimensionless constants [29]. In Eq. $(13)_2$, (a, b, c) are cyclic permutations of $(1, 2, 3)$. For the examples used in this study, only one term is considered in the Ogden strain energy function, i.e. the parameter $N_{mt} = 1$. The shear modulus G_p for this term is set to the shear modulus G and the dimensionless constant $\alpha_p = 2$. This choice of parameters causes the regularized Ogden strain energy function to coincide with the regularized Neo-Hookean strain energy function. The volumetric function is set to $\psi_{vol} = \frac{\kappa}{2}(J-1)^2$, where κ is the bulk modulus.

The other constitutive model is an isotropic elasto-viscoplastic model, based on a multiplicative decomposition of the deformation gradient $\boldsymbol{F} = \boldsymbol{F}^e.\boldsymbol{F}^p$, where $\boldsymbol{F}^e$ and $\boldsymbol{F}^p$ are the elastic and plastic parts, respectively, of the total deformation gradient $\boldsymbol{F}$. Following consequences of frame indifference and isotropy, the free energy has the form $\psi(\boldsymbol{b}^e(\boldsymbol{F}, \boldsymbol{F}^p), \alpha)$ where $\boldsymbol{b}^e$ is the elastic left Cauchy-Green deformation tensor whose eigenvalues are the elastic principal stretches $\lambda^e_a, a = 1, 2, 3$ and α is the accumulated plastic strain. Following the Coleman-Noll procedure gives the Kirchhoff stress tensor $\boldsymbol{\tau}$ as

$$\boldsymbol{\tau} = 2\frac{\partial\psi}{\partial\boldsymbol{b}^e}.\boldsymbol{b}^e \tag{14}$$

which is related to the first Piola-Kirchhoff stress $\boldsymbol{P}$ as $\boldsymbol{P} = \boldsymbol{\tau}.\boldsymbol{F}^{-T}$. The free energy ψ follows the decomposition $\psi(\boldsymbol{b}^e, \alpha) = \mathscr{W}(\boldsymbol{b}^e) + \mathscr{H}(\alpha)$ into a hyperelastic strain energy function $\mathscr{W} = \mathscr{W}_{iso} + \mathscr{W}_{vol}$ and hardening potential $\mathscr{H}$. The isochoric and volumetric parts of the strain energy function $\mathscr{W}$ are set to those used for the hyperelastic model defined above, but in terms of the elastic principal stretches $\lambda^e_a, a = 1, 2, 3$. Linear isotropic strain hardening is assumed, with the hardening potential $\mathscr{H} = \frac{1}{2}K^h\alpha^2$ in terms of the hardening coefficient K^h. To complete the constitutive model, flow rules describing the evolution of internal variables are prescribed in an associative manner by defining a yield function ϕ, chosen as the von Mises yield function, i.e.

$$\phi = \sqrt{\frac{3}{2}}\boldsymbol{s} - \zeta(\alpha) \tag{15}$$

where $\boldsymbol{s} = \boldsymbol{\tau} - 1/3\mathrm{tr}(\boldsymbol{\tau})\boldsymbol{I}$ is the deviatoric part of the Kirchhoff stress tensor $\boldsymbol{\tau}$ and $\zeta(\alpha) = \sigma_y + \partial\mathscr{H}/\partial\alpha$ is the hardening function. Rate effects are accounted for in a Perzyna-type approach, following the model in

Refs. [28,30,31], which defines the following flow rules

$$\begin{aligned} \boldsymbol{A} &= \dot{\gamma}\frac{\partial \phi}{\partial \boldsymbol{\tau}} = \dot{\gamma}\sqrt{\frac{3}{2}}\boldsymbol{n} \\ \dot{\alpha} &= \dot{\gamma} \\ \dot{\gamma} &= \begin{cases} \dfrac{1}{\mu}\left[\left(\sqrt{\dfrac{3}{2}}\dfrac{s}{\zeta}\right)^{\frac{1}{\vartheta}} - 1\right], & \phi \geq 0 \\ 0, & \phi < 0 \end{cases} \end{aligned} \tag{16}$$

where μ is a viscosity parameter (in units of time) and ϑ is a dimensionless rate sensitivity parameter such that the rate-independent von Mises model is recovered from Eq. (16) as $\vartheta \to 0$ or $\mu \to 0$ [28]. The tensor $\boldsymbol{A}$ is defined in terms of $\mathscr{L}_v[\boldsymbol{b}^e]$ – the objective Lie derivative of the elastic left Cauchy-Green deformation tensor – as

$$\boldsymbol{A} = -\frac{1}{2}\mathscr{L}_v[\boldsymbol{b}^e].\boldsymbol{b}^{e-1} \tag{17}$$

Numerical implementation of this constitutive model is carried out following the exponential return mapping algorithm discussed in Appendix A. Details on constitutive modeling of finite deformation elasto-plasticity can be found in Refs. [28,32].

3. Topology optimization

The optimization problem formulation is now presented along with details on the density-based bi-material design parameterization and sensitivity information needed for use with the gradient based optimizer.

3.1. Problem formulation

The intent of this study is to find the optimal layout of a hard stiffness providing phase and soft energy dissipating phase within a given domain so as to dissipate the maximum amount of energy through plastic work. The distribution of material is determined using a density-based parameterization, wherein each element in a discretized domain is assigned a density variable ρ_e representing whether the element contains the energy-dissipating elasto-viscoplastic phase ($\rho_e = 0$) or the stiffness providing hyperelastic phase ($\rho_e = 1$). This density variable is relaxed to be continuous, i.e. $0 \leq \rho_e \leq 1$, so that a computationally intensive integer programming problem is transformed to a more amenable nonlinear programming problem. The plastic work within a design domain over the duration of loading is

$$W^p = \int_t \int_{\Omega_0} \dot{w}^{vp} dV dt \tag{18}$$

where the viscoplastic power density $\dot{w}^{vp}$ is provided by the elasto-viscoplastic phase and is given by making use of Eq. $(16)_1$ as

$$\dot{w}^{vp} = \boldsymbol{\tau}^{VP} : \boldsymbol{A} = \dot{\gamma}\sqrt{\frac{3}{2}}\boldsymbol{\tau}^{VP} : \boldsymbol{n} \tag{19}$$

Here $\boldsymbol{\tau}^{VP}$ and $\boldsymbol{n}$ are the Kirchhoff stress and flow vector in the viscoplastic phase. Maximizing W^p as the objective function, while constraining the volume of energy dissipating elasto-viscoplastic phase to be below a prescribed volume fraction V_f results in the following optimization problem

$$\begin{aligned} &\min_x \quad f_0(\boldsymbol{x}) = -W^p \\ &\text{s.t.} \quad f_1(\boldsymbol{x}) = 1 - \frac{1}{V}\sum_{e=1}^{n_{ele}} \rho_e(\boldsymbol{x}) v_e - V_f \leq 0 \\ &\boldsymbol{R}^k\left(\widehat{\boldsymbol{u}}^k, \widehat{\boldsymbol{u}}^{k-1}, \boldsymbol{c}^k, \boldsymbol{c}^{k-1}, \boldsymbol{\rho}(\boldsymbol{x})\right) = \boldsymbol{0}, \quad k = 1, 2, \ldots, n \\ &\boldsymbol{H}^k\left(\widehat{\boldsymbol{u}}^k, \widehat{\boldsymbol{u}}^{k-1}, \boldsymbol{c}^k, \boldsymbol{c}^{k-1}, \boldsymbol{\rho}(\boldsymbol{x})\right) = \boldsymbol{0}, \quad k = 1, 2, \ldots, n \\ &\boldsymbol{0} \leq \boldsymbol{x} \leq \boldsymbol{1} \end{aligned} \tag{20}$$

where V is the total volume of the design domain, and v_e is the volume of element e. A density filtering procedure is used to ensure mesh-independency and control the length scale of topological features [33–35]. In this case, the design variables $\boldsymbol{x}$ are linearly mapped by the density filtering operator to the vector $\boldsymbol{\rho}$ of density variables containing the weighted average of the design variables of neighboring elements.

The system represented in Eq. (20) is a PDE-constrained optimization problem wherein constraint $\boldsymbol{R}^k = \boldsymbol{0}$ represents the global equations of motion and $\boldsymbol{H}^k = \boldsymbol{0}$ represents the local integration point constitutive equations. These constraints are enforced implicitly through finite element analysis (FEA) in a nested approach where the design variables $\boldsymbol{x}$ are updated by the optimizer and then used in FEA [36]. As such, constraints $\boldsymbol{R}^k = \boldsymbol{0}$ and $\boldsymbol{H}^k = \boldsymbol{0}$ in Eq. (20) are enforced for each time step k of the dynamic FEA. Once FEA has terminated, the objective and constraint functions are evaluated. At step k, primary and internal variables are updated using previous step and current step information and so the implicit constraints are functionally dependent on this data, represented by a set of global variables $\widehat{\boldsymbol{u}}$ and local variables $\boldsymbol{c}$. Furthermore, these constraints are dependent on the density variables $\boldsymbol{\rho}$ through material interpolation, as discussed in the following section. Hence, they have the functional form shown in Eq. (20).

3.2. Bi-material interpolation scheme

To optimize placement of the desired material phases using a density-based parameterization, a material interpolation scheme is needed for representing intermediate behavior between different phenomenological models in a consistent way. Moreover, this scheme should be able to ensure that density values in the final design correspond to distinct material phases. Extensions of the SIMP [37] approach to consider multiple material phases assume that a single constitutive relation represents the behavior of each phase so that interpolation is carried out between values of the material parameters, see e.g. Refs. [23,38]. However, when considering material phases with distinct phenomenological behavior (i.e. elastic and elastoplastic) each phase relies on a different set of internal variables whose evolution is controlled by certain material parameters. Hence, there is no one-to-one correspondence between sets of material parameters. Material mixing rules, on the other hand, allow for every material point to consider a distinct set of constitutive relations for each phase and utilize assumptions on overall stress and strain behavior to provide the composite response. Classic mixing rules are the Voigt [39] and Reuss [40] approaches, which have been employed in hybridized form to carry out multimaterial topology optimization by Swan and Kosaka [9] and Swan and Aurora [41]. In the small strain regime, Voigt mixing rules provide an upper bound on the stiffness behavior of composites by assuming that the material phases are arranged in parallel, resulting – when loaded axially – in a uniform strain state throughout the composite but differing stress states within the individual phases. Alternatively, Reuss mixing rules provide a lower bound by assuming materials are arranged in series, which results in a uniform composite stress state but differing strain states. The finite deformation analogue to the Voigt assumption is Taylor's assumption [42]. This also provides an upper bound by postulating material phases as being in parallel, with the

resulting uniform composite strain state and differing individual stress states.

Taylor's assumption is taken as the basis for formulating the bi-material interpolation scheme utilized in this work. It states that for a uniform strain state (defined by $\boldsymbol{F}$), the first Piola-Kirchhoff stress in the composite material with m constituient phases is

$$\boldsymbol{P} = \sum_{i}^{m} \phi_i \boldsymbol{P}_i(\boldsymbol{F}) \tag{21}$$

where ϕ_i is the volume fraction of phase i. As the first Piola-Kirchhoff stress is derived in terms of a free energy function ψ ($\boldsymbol{P} = \partial\psi / \partial\boldsymbol{F}$), this relation is equivalent to

$$\psi = \sum_{i}^{m} \phi_i \psi_i(\boldsymbol{F}) \tag{22}$$

Taking Eq. (22) as inspiration, the free energy for an element with density variable $\rho_e \in [0, 1]$ is defined by mixing the scaled free energies of each phase, with the scaling factors reflecting the material volume fraction as a function of ρ_e. Hence

$$\psi^e = \chi_H(\rho_e)\psi_{HE} + \chi_S(\rho_e)\psi_{VP} \tag{23}$$

where ψ_{VP} and ψ_{HE} are the free energy functions of the elasto-viscoplastic phase and hyperelastic phase, respectively, which are scaled by the factors χ_H and χ_S.

Taylor's assumption provides physically motivated estimates of mixed material behavior, but violates stress equilibrium. Hence, it does not provide physically realizable material behavior for mixed phases ($0 < \rho_e < 1$). In order to ensure that the final topology is free of intermediate density values which correspond to these physically unrealizable materials, penalization in the spirit of the SIMP method is utilized, so that the scaling factors χ_H and χ_S include a penalization parameter p, i.e.

$$\begin{aligned} \chi_H(\rho_e) &= \rho_e^p \\ \chi_S(\rho_e) &= 1 - \rho_e^p \end{aligned} \tag{24}$$

This penalization provides the proper scaling of the stress-strain behavior between the two phases, which can be seen in Fig. 1a – where the stress-strain behavior resulting from a one element uniform extension test using Eqns. (23) and (24) with $p = 3$ and different values of ρ_e is shown. However, Fig. 1b shows that intermediate density values result in essentially the same plastic work as the purely elasto-viscoplastic phase. Hence, while the Kirchhoff stress $\boldsymbol{\tau}^{VP}$ is scaled by χ_S due to its definition in terms of the strain energy ψ_{VP} (Eqn. (23) and (14)) this scaling clearly is not enough to encourage the optimizer to push element density variables ρ_e to 0 (elasto-viscoplastic phase) or 1 (hyperelastic phase). In order to ensure that the plastic work in elements with intermediate density values is appropriately penalized, the tensor $\boldsymbol{A}$ in Eq. (19) is scaled such that the viscoplastic power density becomes

$$\dot{w}^{vp} = \boldsymbol{\tau}^{VP} : (\chi_A \boldsymbol{A}) = \chi_A \dot{\gamma} \sqrt{\frac{3}{2}} \boldsymbol{\tau}^{VP} : \boldsymbol{n} \tag{25}$$

where $\chi_A = 1 - \rho_e^{p_A}$ and p_A is an extra penalization parameter. Inserting this into Eq. (18) and using the trapezoid rule gives the discrete expression used to evaluate the plastic work objective function

$$W^p \approx \sum_{k=1}^{n} \left(\sum_{e=1}^{n_{ele}} \left(\sum_{r=1}^{n_{ipt}} \left(w_r \chi_A \sqrt{\frac{3}{2}} \Delta\gamma_{e_r}^k \boldsymbol{\tau}_{e_r}^{VP^k} : \boldsymbol{n}_{e_r}^k \right) \right) \right) \tag{26}$$

Fig. 1c and d show the stress-strain behavior and plastic work history when the viscoplastic power density is defined as in Eq. (25) with $p_A = 1$. Clearly, the inclusion of the scaling factor χ_A results in a significant reduction in the plastic work when intermediate densities are considered.

Finally, as inertia effects depend on the mass density of the different materials, the reference mass density ρ_0 in the definition of the element mass matrix (Eq. (5)) is set to 1 and the resulting normalized mass matrix is scaled by the density scaling factor

$$\chi_\rho = \rho_e \rho_0^{HE} + (1 - \rho_e)\rho_0^{VP} \tag{27}$$

which is simply defined in terms of the volume fraction of the two phases. Here, ρ_0^{HE} is the reference mass density of the hard hyperelastic phase and ρ_0^{VP} is the reference mass density of the soft elasto-viscoplastic phase.

3.3. Sensitivity analysis

Accurate sensitivity information is paramount to the ability of gradient-based optimizers to consistently and robustly find optimal solutions. In the context of PDE constrained optimization problem in Eq. (20), sensitivity calculations are complicated by the fact that they must account for the implicit constraints $\boldsymbol{R}^k = \boldsymbol{0}$ and $\boldsymbol{H}^k = \boldsymbol{0}$ at each time step k. The formulation of a general adjoint sensitivity analysis framework for problems governed by such PDEs is covered in detail in Ref. [27]. For a given response function f with the general functional form $f(\boldsymbol{x}) = F(\widehat{\boldsymbol{u}}^1, \ldots, \widehat{\boldsymbol{u}}^n, \boldsymbol{c}^1, \ldots, \boldsymbol{c}^n, \boldsymbol{\rho}(\boldsymbol{x}))$, the derivative with respect to the design variables $\boldsymbol{x}$ is sought. As application of the density filter is straightforwardly accounted for by applying the chain rule, the derivative $df/d\boldsymbol{\rho}$ must be calculated. Following the approach in Ref. [27], adjoint sensitivity analysis proceeds by solving the following system for the adjoint variables $\boldsymbol{\lambda}^k$ and $\boldsymbol{\mu}^k$

$$\begin{aligned} n^{th}\ step: & \begin{cases} \dfrac{\partial F}{\partial \widehat{\boldsymbol{u}}^n} + \boldsymbol{\lambda}^{n^T} \dfrac{\partial \boldsymbol{R}^n}{\partial \widehat{\boldsymbol{u}}^n} + \boldsymbol{\mu}^{n^T} \dfrac{\partial \boldsymbol{H}^n}{\partial \widehat{\boldsymbol{u}}^n} = \boldsymbol{0} \\ \dfrac{\partial F}{\partial \boldsymbol{c}^n} + \boldsymbol{\lambda}^{n^T} \dfrac{\partial \boldsymbol{R}^n}{\partial \boldsymbol{c}^n} + \boldsymbol{\mu}^{n^T} \dfrac{\partial \boldsymbol{H}^n}{\partial \boldsymbol{c}^n} = \boldsymbol{0} \end{cases} \\ k^{th}\ step: & \begin{cases} \dfrac{\partial F}{\partial \widehat{\boldsymbol{u}}^k} + \boldsymbol{\lambda}^{k+1^T} \dfrac{\partial \boldsymbol{R}^{k+1}}{\partial \widehat{\boldsymbol{u}}^k} + \boldsymbol{\mu}^{k+1^T} \dfrac{\partial \boldsymbol{H}^{k+1}}{\partial \widehat{\boldsymbol{u}}^k} + \boldsymbol{\lambda}^{k^T} \dfrac{\partial \boldsymbol{R}^k}{\partial \widehat{\boldsymbol{u}}^k} + \boldsymbol{\mu}^{k^T} \dfrac{\partial \boldsymbol{H}^k}{\partial \widehat{\boldsymbol{u}}^k} = \boldsymbol{0} \\ \dfrac{\partial F}{\partial \boldsymbol{c}^k} + \boldsymbol{\lambda}^{k+1^T} \dfrac{\partial \boldsymbol{R}^{k+1}}{\partial \boldsymbol{c}^k} + \boldsymbol{\mu}^{k+1^T} \dfrac{\partial \boldsymbol{H}^{k+1}}{\partial \boldsymbol{c}^k} + \boldsymbol{\lambda}^{k^T} \dfrac{\partial \boldsymbol{R}^k}{\partial \boldsymbol{c}^k} + \boldsymbol{\mu}^{k^T} \dfrac{\partial \boldsymbol{H}^k}{\partial \boldsymbol{c}^k} = \boldsymbol{0} \end{cases} \\ & k = n-1,\ \ldots,\ 2,\ 1 \end{aligned} \tag{28}$$

This system is solved by starting at step n and ending at step **1** and after its solution, the sensitivity $df/d\boldsymbol{\rho}$ is given as

$$\frac{df}{d\boldsymbol{\rho}} = \frac{\partial F}{\partial \boldsymbol{\rho}} + \sum_{k=1}^{n} \left(\boldsymbol{\lambda}^{k^T} \frac{\partial \boldsymbol{R}^k}{\partial \boldsymbol{\rho}} + \boldsymbol{\mu}^{k^T} \frac{\partial \boldsymbol{H}^k}{\partial \boldsymbol{\rho}} \right) \tag{29}$$

Thus, the following derivatives are needed to evaluate Eqns. (28) and (29):

$$\text{For } \boldsymbol{R}^k: \begin{cases} \dfrac{\partial \boldsymbol{R}^k}{\partial \boldsymbol{\rho}} \\ \dfrac{\partial \boldsymbol{R}^k}{\partial \widehat{\boldsymbol{u}}^k} \\ \dfrac{\partial \boldsymbol{R}^k}{\partial \widehat{\boldsymbol{u}}^{k-1}} \\ \dfrac{\partial \boldsymbol{R}^k}{\partial \boldsymbol{c}^k} \\ \dfrac{\partial \boldsymbol{R}^k}{\partial \boldsymbol{c}^{k-1}} \end{cases}, \text{For } \boldsymbol{H}^k: \begin{cases} \dfrac{\partial \boldsymbol{H}^k}{\partial \boldsymbol{\rho}} \\ \dfrac{\partial \boldsymbol{H}^k}{\partial \widehat{\boldsymbol{u}}^k} \\ \dfrac{\partial \boldsymbol{H}^k}{\partial \widehat{\boldsymbol{u}}^{k-1}} \\ \dfrac{\partial \boldsymbol{H}^k}{\partial \boldsymbol{c}^k} \\ \dfrac{\partial \boldsymbol{H}^k}{\partial \boldsymbol{c}^{k-1}} \end{cases}, \text{For } F: \begin{cases} \dfrac{\partial F}{\partial \boldsymbol{\rho}} \\ \dfrac{\partial F}{\partial \widehat{\boldsymbol{u}}^k} \\ \dfrac{\partial F}{\partial \boldsymbol{c}^k} \end{cases} \tag{30}$$

These are obtained by specifying the set of global $\widehat{\boldsymbol{u}}$ and local $\boldsymbol{c}$ state variables and their corresponding constraint equations. For the problems considered in this study, the global state variables and constraints are the displacement, velocity and acceleration degrees of freedom for the HHT

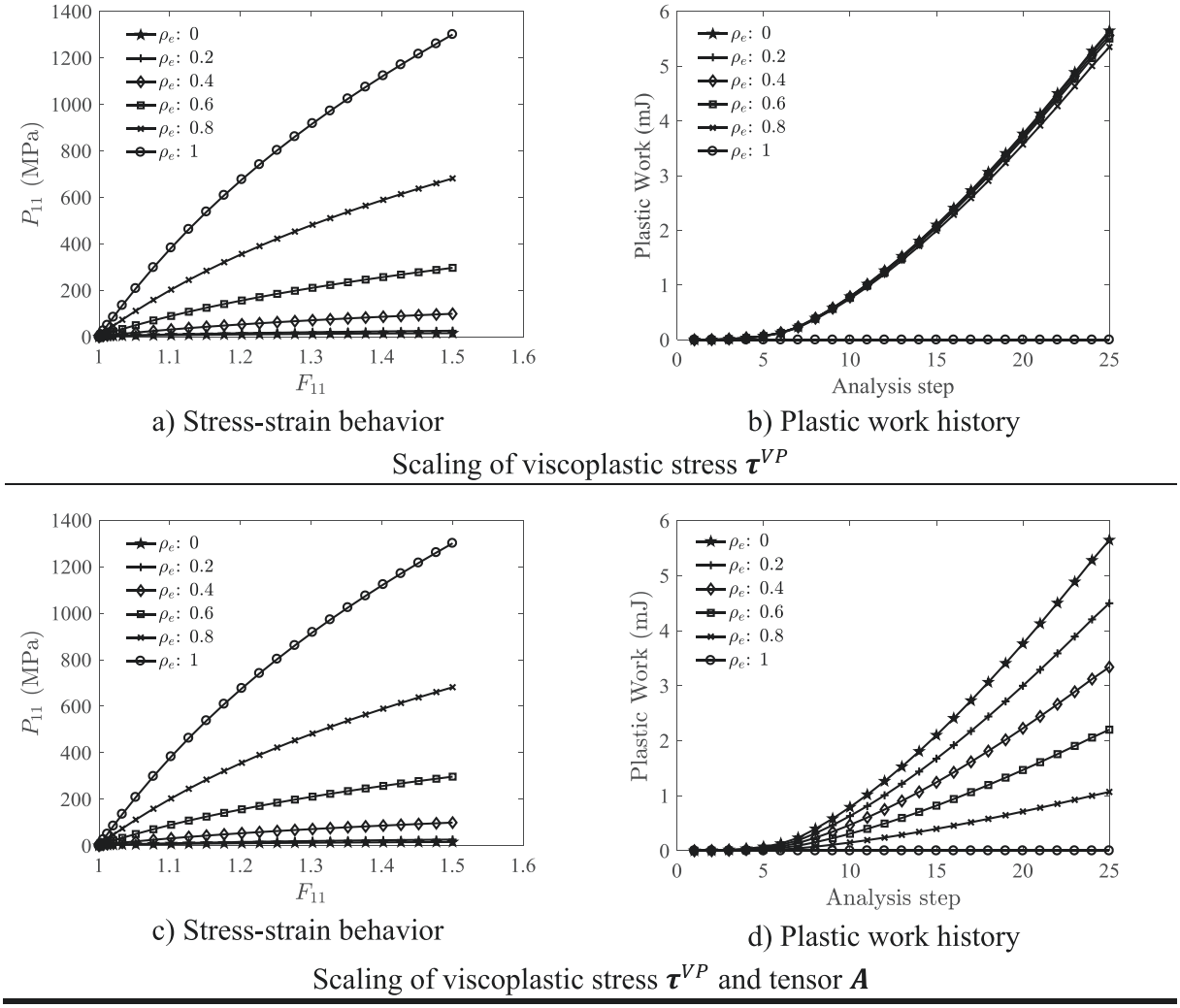

Fig. 1. Stress-strain behavior and plastic work history for one element uniform extension test using bi-material interpolation scheme with only scaling of viscoplastic stress and with scaling of both viscoplastic stress τ^{VP} and tensor A.

time integration algorithm discussed in Section 2.1. Hence, $\hat{u}^k = [u^k, v^k, a^k]^T$, and the corresponding global constraints are the residual equation Eq. (9) and the update equations Eq. (11) rewritten here as

$$R^k = \begin{bmatrix} R_u^k \\ R_v^k \\ R_a^k \end{bmatrix} = \begin{bmatrix} \overset{n_{ele}}{\mathcal{A}}_{e=1}\left(\tilde{F}_{int}^{e^k} - F_{ext}^{e^k}\right) \\ v^k - \tilde{v}^k - \frac{\gamma}{\beta\Delta t}\left(u^k - \tilde{u}^k\right) \\ a^k - \frac{1}{\beta\Delta t^2}\left(u^k - \tilde{u}^k\right) \end{bmatrix} \tag{31}$$

$$\tilde{F}_{int}^{e^k} = (1+\alpha)F_{int}^{e^k} - \alpha F_{int}^{e^{k-1}} + \frac{\chi_\rho}{\beta\Delta t^2} M_e\left(u_e^k - \tilde{u}_e^k\right)$$

$$\tilde{u}^k = u^{k-1} + \Delta t v^{k-1} + \frac{\Delta t^2}{2}(1-2\beta)a^{k-1}$$

$$\tilde{v}^k = v^{k-1} + (1-\gamma)\Delta t a^{k-1}$$

where the element internal force vector is $F_{int}^{e^k} = \sum_{r=1}^{n_{ipt}} w_r r_{e_r}^{k^{a-1}} B_{e_r}^T \bar{P}_{e_r}^k$ following Eq. (6). Here, $r_{e_r}^k$ is the deformation gradient ratio defined in Eq. (4) for integration point r, $a = 1/2$ for the plane strain case and w_r is the weight of the r^{th} integration point. For the four node plane strain F-bar elements with $n_{ipt} = 4$ integration points and unit thickness employed in this study, the chosen local variables c^k are represented in vector form as

$$c^k = \begin{bmatrix} c_1^k \\ \vdots \\ c_{n_{ele}}^k \end{bmatrix} \text{ with } c_e^k = \begin{bmatrix} c_{e_1}^k \\ c_{e_2}^k \\ c_{e_3}^k \\ c_{e_4}^k \end{bmatrix} \text{ and } c_{e_r}^k = \begin{bmatrix} b_{e_r}^{e^k} \\ \alpha_{e_r}^k \\ \Delta\gamma_{e_r}^k \end{bmatrix} \tag{32}$$

The local constraint equations corresponding to these variables thus have the form

$$H^k = \begin{bmatrix} H_1^k \\ \vdots \\ H_{n_{ele}}^k \end{bmatrix} = 0 \text{ with } H_e^k = \begin{bmatrix} H_{e_1}^k \\ H_{e_2}^k \\ H_{e_3}^k \\ H_{e_4}^k \end{bmatrix} \text{ and } H_{e_r}^k = \begin{bmatrix} h_{e_{r1}}^k \\ h_{e_{r2}}^k \\ h_{e_{r3}}^k \end{bmatrix} \tag{33}$$

and the residual equations $H_{e_r}^k$ at each integration point r follow from the constitutive algorithm discussed in Appendix A. For a given integration point at the elastic step, these equations are

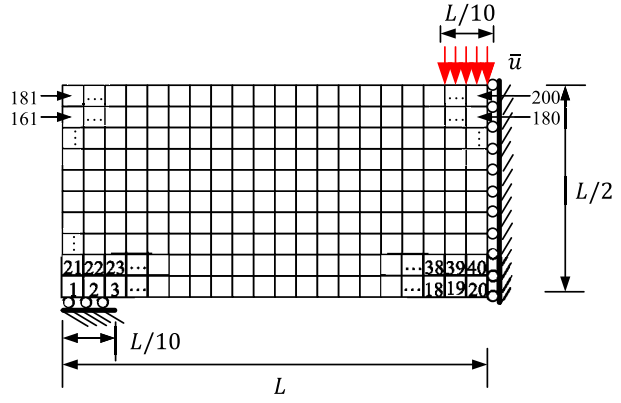

Fig. 2. Design domain and element numbering of half-beam bending problem for sensitivity verification.

$$\boldsymbol{H}_{e_r}^k = \begin{cases} \boldsymbol{h}_{e_{r1}}^k = \boldsymbol{b}_{e_r}^{e^k} - \boldsymbol{b}_{e_r}^{e,tr} = 0 \\ h_{e_{r2}}^k = \alpha_{e_r}^k - \alpha_{e_r}^{k-1} = 0 \\ h_{e_{r3}}^k = \Delta\gamma_{e_r}^k = 0 \end{cases} \tag{34}$$

and for a given integration point at the viscoplastic step, they are

$$\boldsymbol{H}_{e_r}^k = \begin{cases} \boldsymbol{h}_{e_{r1}}^k = \boldsymbol{b}_{e_r}^{e^k} - \boldsymbol{b}_{e_r}^{e,tr}.\exp\left[-2\Delta t \boldsymbol{A}_{e_r}^k\right] = \boldsymbol{0} \\ h_{e_{r2}}^k = \alpha_{e_r}^k - \alpha_{e_r}^{k-1} - \Delta\gamma_{e_r}^k = 0 \\ h_{e_{r3}}^k = \sqrt{\frac{3}{2}}\boldsymbol{s}_{e_r}^{VP^k}\left(\frac{\Delta t}{\mu\Delta\gamma_{e_r}^k + \Delta t}\right)^{\vartheta} - \zeta(\alpha_{e_r}^k) = \boldsymbol{0} \end{cases} \tag{35}$$

where $\Delta t = t_k - t_{k-1}$. The derivatives in Eq. (30) needed to complete the sensitivity analysis based on these definitions are given in Appendix B.

4. Design examples

Design examples are now carried out to demonstrate the capability of the developed topology optimization framework and present insights into how the arrangement of different material phases can lead to improvements in energy dissipation capacity. In all of the following examples, the material parameters of the soft elasto-viscoplastic phase are set to $E = 3300$ MPa, $\nu = 0.33$, $\sigma_y = 105$ MPa and $K^h = 300$ MPa. The bulk and shear moduli of the hard hyperelastic phase are set to $\kappa = 55,000$ MPa and $G = 1,100$ MPa, resulting in nearly incompressible behavior ($E \approx 3.278 \times 10^3$ MPa, $\nu \approx 0.49$). Design domains are dis-

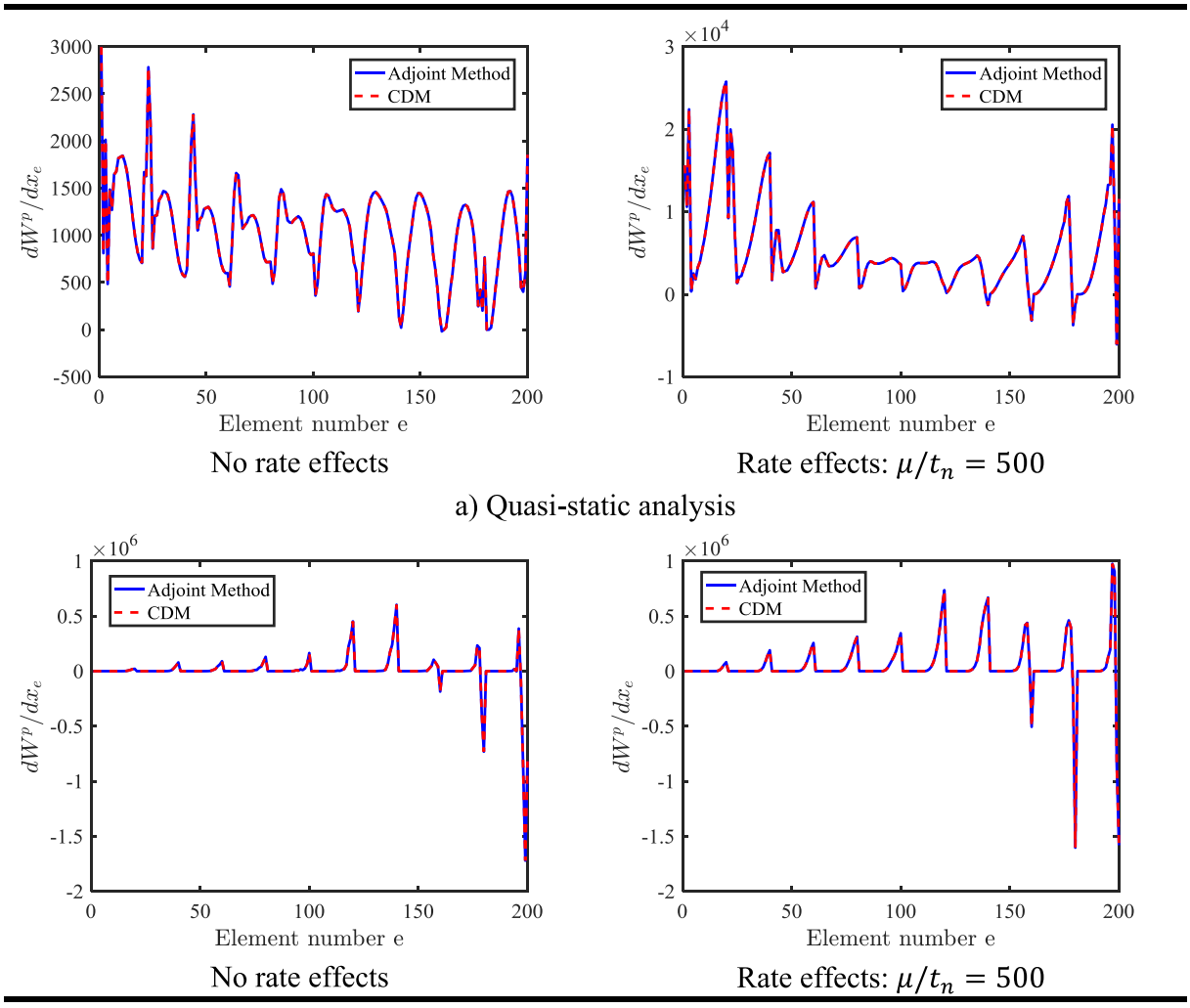

Fig. 3. Comparison of sensitivity values obtained using the adjoint method and CDM with $\Delta h = 10^{-5}$ for quasi-static and dynamic analyses using half-beam bending problem with and without rate effects.

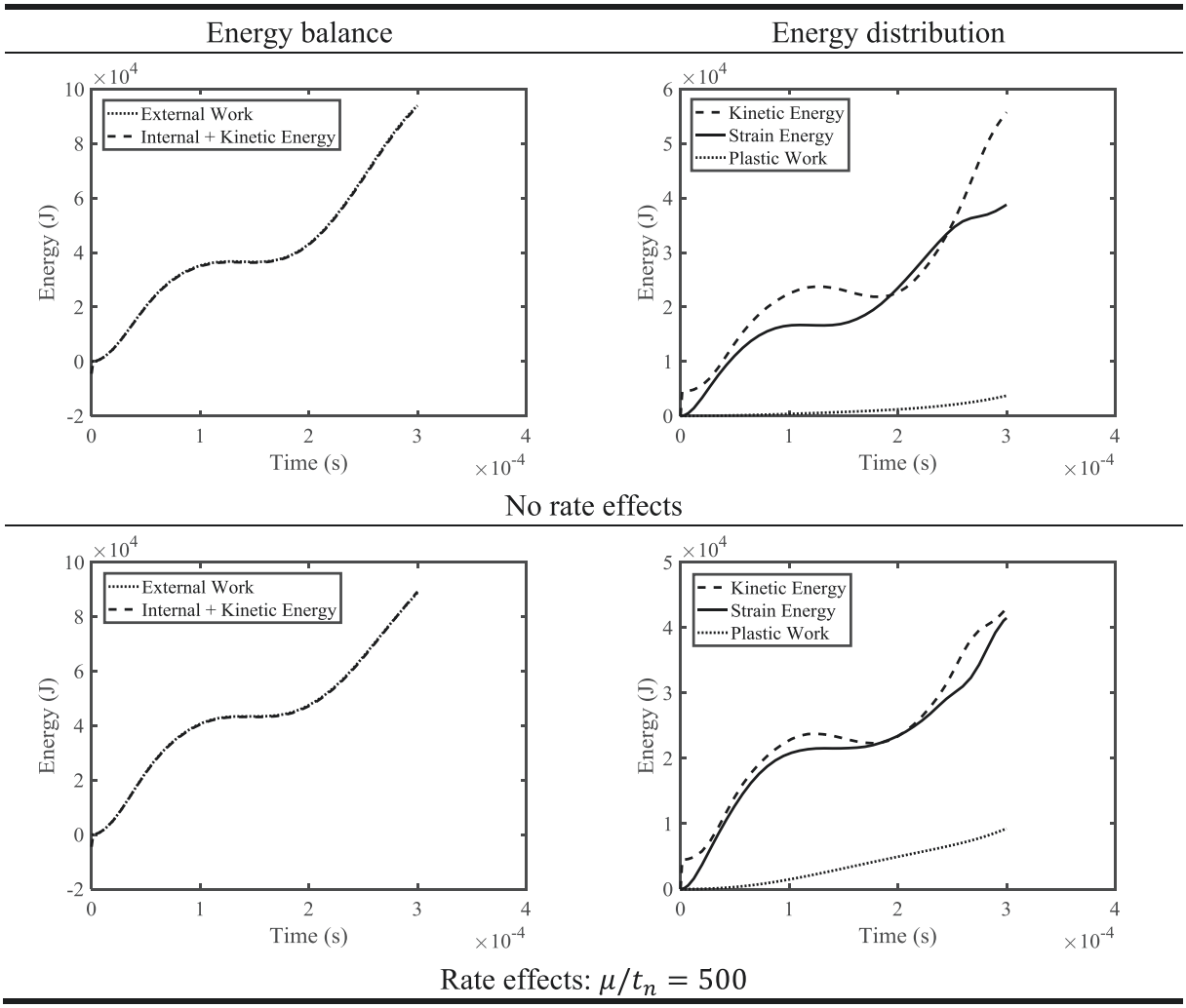

Fig. 4. Energy balance and distribution for dynamic analysis of half-beam bending problem with and without rate effects.

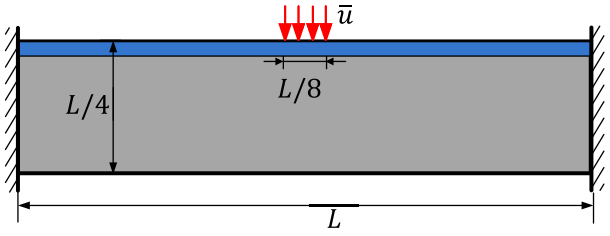

Fig. 5. Clamped beam problem configuration.

cretized using four node plane strain F-bar elements with unit thickness. The Hilber-Hughes-Taylor algorithm detailed in Section 2.1 is used to carry out time integration, with adaptive time stepping following the strategy in Ref. [43] and convergence criterion based on the global energy residual, $\text{abs}(\boldsymbol{R}^T \boldsymbol{\Delta}\widehat{\boldsymbol{u}}) \leq 10^{-10}$. As a change in the time step can introduce numerical high frequency vibrations into the model, the damping parameter α for the HHT algorithm is set to a low value of $\alpha = -0.05$. The other algorithmic parameters β and γ are defined in terms of this damping parameter as $\beta = 1/4(1-\alpha)^2$ and $\gamma = 1/2 - \alpha$, following [26]. Using this numerical scheme, finite element analysis was stable throughout the optimization process for all design examples. Optimization is carried out using the Method of Moving Asymptotes (MMA) [44] with default algorithmic parameters and terminated after 150 total iterations. Initial designs consist of a uniform distribution of design variables x_e set to the prescribed volume fraction. The filter radius utilized is $r_{min} = 3 \times ms$ where ms is the size of each element in the uniform mesh and in all of the figures showing optimized composite topologies, the soft elasto-viscoplastic phase is shown in red while the hard hyperelastic phase is shown in blue. The in-house Matlab based finite element library *CPSSL-FEA* developed at the University of Notre Dame is used to perform both the optimization and FEA.

4.1. Sensitivity verification

To ensure correct implementation of the sensitivity analysis discussed in Section 3.3, a verification study is performed. Analytical values obtained using the adjoint method are compared to the values obtained numerically using the central difference method (CDM), which computes the sensitivity of the plastic work W^p with respect to design variable x_e as follows

$$\frac{dW^p(\boldsymbol{x})}{dx_e} \approx \frac{W^p(\boldsymbol{x} + \Delta\boldsymbol{h}) - W^p(\boldsymbol{x} - \Delta\boldsymbol{h})}{2\Delta h} \tag{36}$$

Here $\Delta\boldsymbol{h}$ is a vector containing all zeros except at the component corresponding to x_e, which has the perturbation value Δh, here taken as 10^{-5}. Sensitivity verification is performed for each elemental design variable of the half-beam bending example discretized in a 20×10 mesh

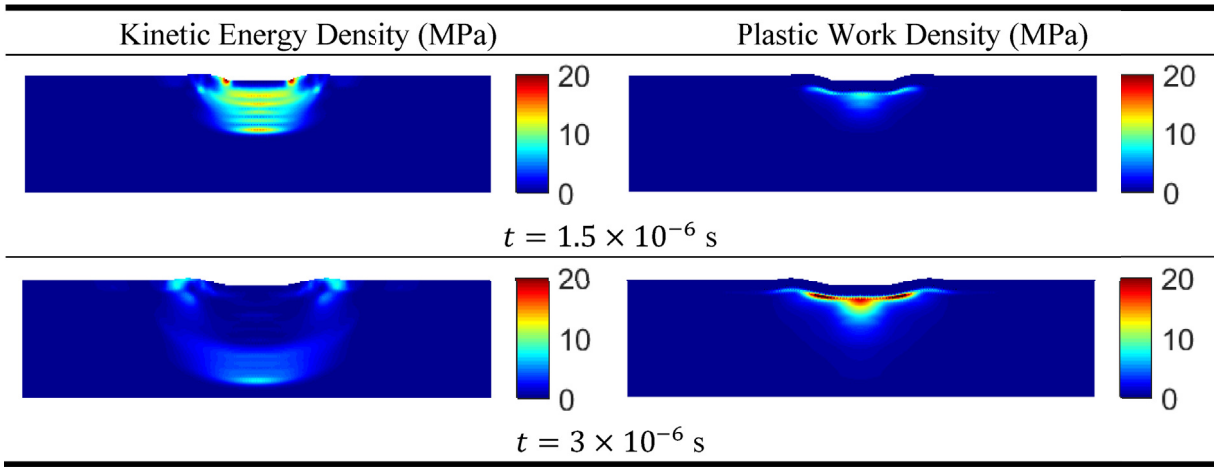

Fig. 6. Snapshots of energy density distributions in deformed configuration at different times during dynamic analysis of clamped beam problem using a uniform distribution of elasto-viscoplastic phase with hyperelastic buffer layer and no rate effects.

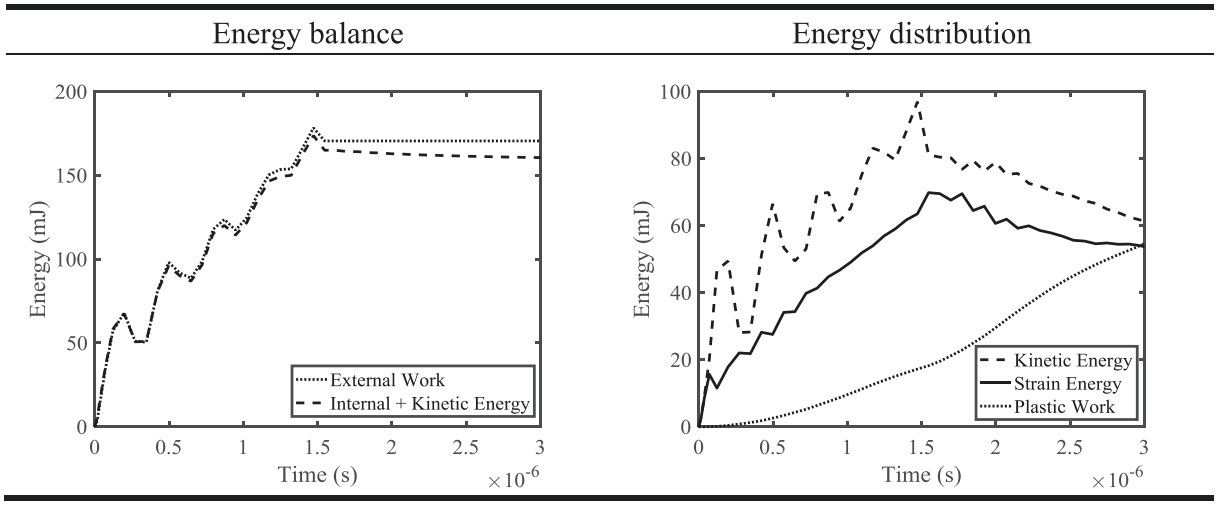

Fig. 7. Energy balance and distribution for dynamic analysis of clamped beam problem using a uniform distribution of elasto-viscoplastic phase with hyperelastic buffer layer and no rate effects.

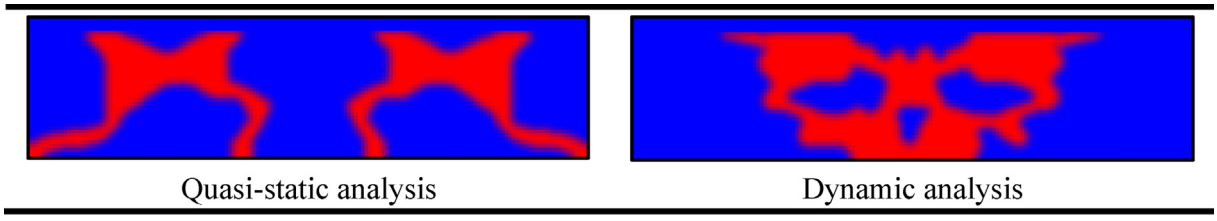

Fig. 8. Optimized topologies for clamped beam problem under quasi-static and dynamic analysis with volume fraction $V_f = 0.3$ and no rate effects.

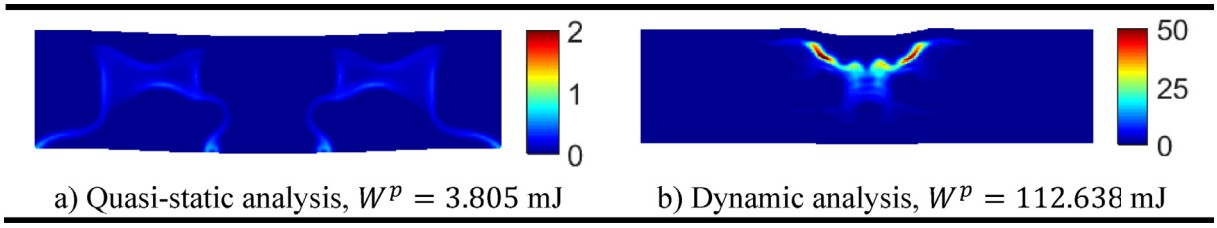

Fig. 9. Distribution of plastic work density (MPa) in deformed configuration at $t = 3 \times 10^{-6}$ s for optimized topologies obtained under quasi-static and dynamic analysis with volume fraction $V_f = 0.3$ and no rate effects.

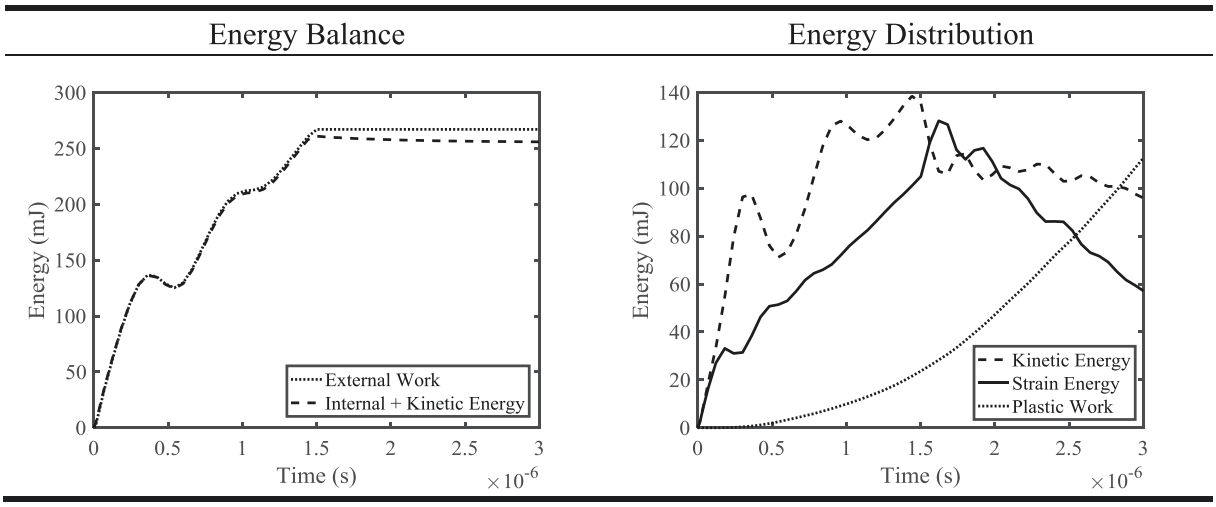

Fig. 10. Energy balance and distribution for optimized topology obtained using dynamic analysis with volume fraction $V_f = 0.3$ and no rate effects.

with elements numbered as shown in Fig. 2 and length $L = 2000$ mm. All design variables x_e are assigned a value of 0.5 and no density filter is considered so that $\boldsymbol{\rho} = \boldsymbol{x}$. The sensitivity of the total plastic work W^P is calculated using the adjoint method and CDM for two cases. In the first case no rate effects are considered in the elasto-viscoplastic phase (i.e. the viscoplastic model parameter ϑ is set to 0 to return the rate-independent von Mises model) while the second case considers rate effects using a ratio between the viscosity parameter and total deformation time $\mu/t_n = 500$, corresponding to a high effective rate.

These two cases are first considered without inertia effects – i.e. the reference mass density of both material phases is set to 0 – and with the prescribed displacement $\overline{u} = 250$ mm applied monotonically. Fig. 3a shows the sensitivity values obtained for this quasi-static analysis using the adjoint method and CDM, and it can be seen that these values match closely. Next, the two cases are considered using a dynamic analysis with the reference mass density of the elasto-viscoplastic phase set to $\rho_0^{VP} = 900$ kg/m^3 and the reference mass density of the hyperelastic phase set to $\rho_0^{HE} = 1,200$ kg/m^3. The prescribed displacement $\overline{u}$ is applied in a half-period sinusoidal pulse, i.e. $\overline{u}(t) = u_{max} \sin(2\pi t/T)$ with the period $T = 2 \times t_n$, final analysis time $t_n = 3 \times 10^{-4}$ s, and maximum displacement amplitude $u_{max} = 100$ mm. The sensitivity values obtained for this dynamic analysis using the adjoint method and CDM are shown in Fig. 3b, where they again are seen to match very closely, thus verifying correct implementation of the sensitivity analysis.

Fig. 4 shows the total external work and sum of the internal and kinetic energies throughout the dynamic analysis along with the distribution of energy into kinetic energy, strain energy and plastic work, for both cases. It can be seen from the distribution of energies that the consideration of rate effects changes how energy is distributed within the system. It can also be seen that the external work (i.e. the total energy input into the system) matches the sum of internal and kinetic energies for both cases, which serves to verify correct implementation of the HHT

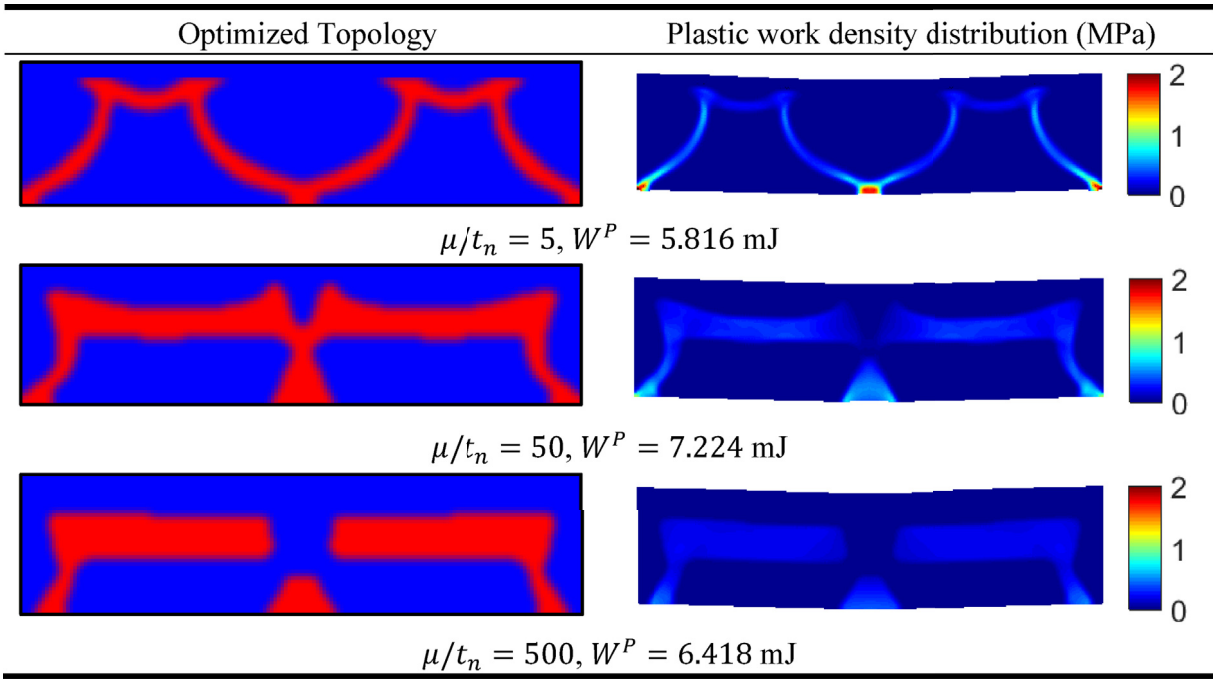

Fig. 11. Optimized topologies and distributions of plastic work density in deformed configuration for clamped beam problem under quasi-static analysis with volume fraction $V_f = 0.3$ and different viscoplastic rate effects.

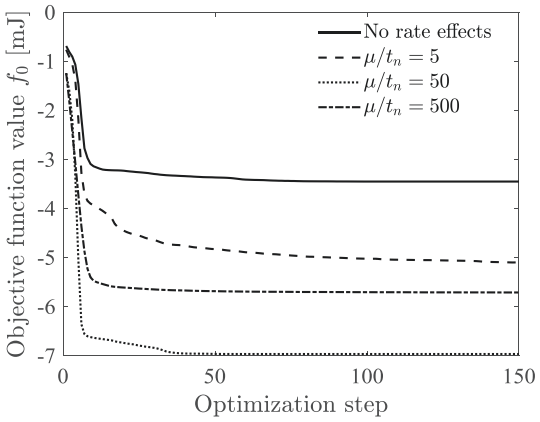

Fig. 12. Convergence curves for clamped beam problem under quasi-static analysis with volume fraction $V_f = 0.3$ and different viscoplastic rate effects.

time integration scheme.

4.2. Inertia effects

The influence of inertia effects on optimized designs is first investigated by considering the clamped beam domain used in Ref. [24] and shown in Fig. 5, where $L = 20$ mm and a 160×40 mesh is used for discretization. The prescribed displacement $\overline{u}$ is applied monotonically over a time period of t_0 and then held constant for another time period of t_0, with $t_0 = 1.5 \times 10^{-6}$ s, so that the final analysis time $t_n = 3\times 10^{-6}$ s. This domain is first subject to dynamic analysis using a uniform distribution of the soft elasto-viscoplastic phase with $\vartheta = 0$ to suppress rate effects. In order to avoid localization of plastic flow near the nodes where displacement is applied, a buffer layer of hyperelastic phase five elements thick is placed at the top of the design domain (indicated by the blue region in Fig. 5). The prescribed displacement $\overline{u}$ is set to 0.25 mm and the reference mass densities of the material phases are $\rho_0^{VP} = 900$ kg/m^3 and $\rho_0^{HE} = 1,200$ kg/m^3. Snapshots of the resulting kinetic energy and plastic work density distributions at $t = 1.5 \times 10^{-6}$ s and $t = 3\times 10^{-6}$ s are shown in Fig. 6.

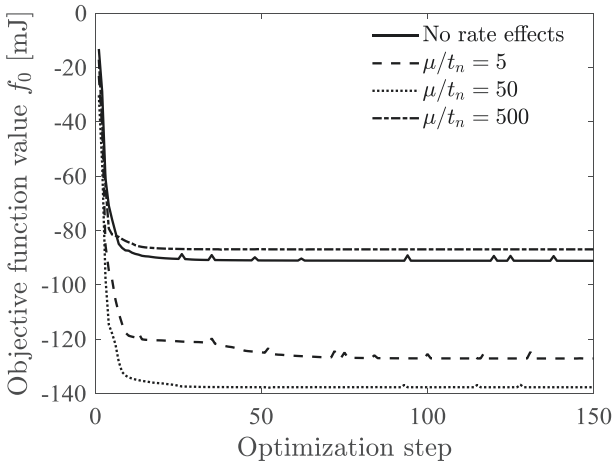

Fig. 14. Convergence curves for clamped beam problem under dynamic analysis with volume fraction $V_f = 0.3$ and different viscoplastic rate effects.

The kinetic energy density snapshots reveal that applying the prescribed displacement at this rate causes a shock wave to propagate through the domain when inertia effects are included. This wave continues to propagate as the prescribed displacement is held constant, causing more material to yield and spreading the plastic work further into the domain, as observed in the plastic work density snapshots. The total external work and sum of the internal and kinetic energies as well as the distribution into kinetic energy, strain energy and plastic work is shown in Fig. 7. Here it can be seen that there are oscillations as the shock wave passes through the hyperelastic buffer layer and into the elasto-viscoplastic domain since there is a mechanical impedance mismatch between these two phases. Some of the high frequency reflections are damped out numerically through the parameter α in the HHT algorithm, causing the external work to be slightly greater than the sum of the internal and kinetic energies, with the difference equal to this numerical

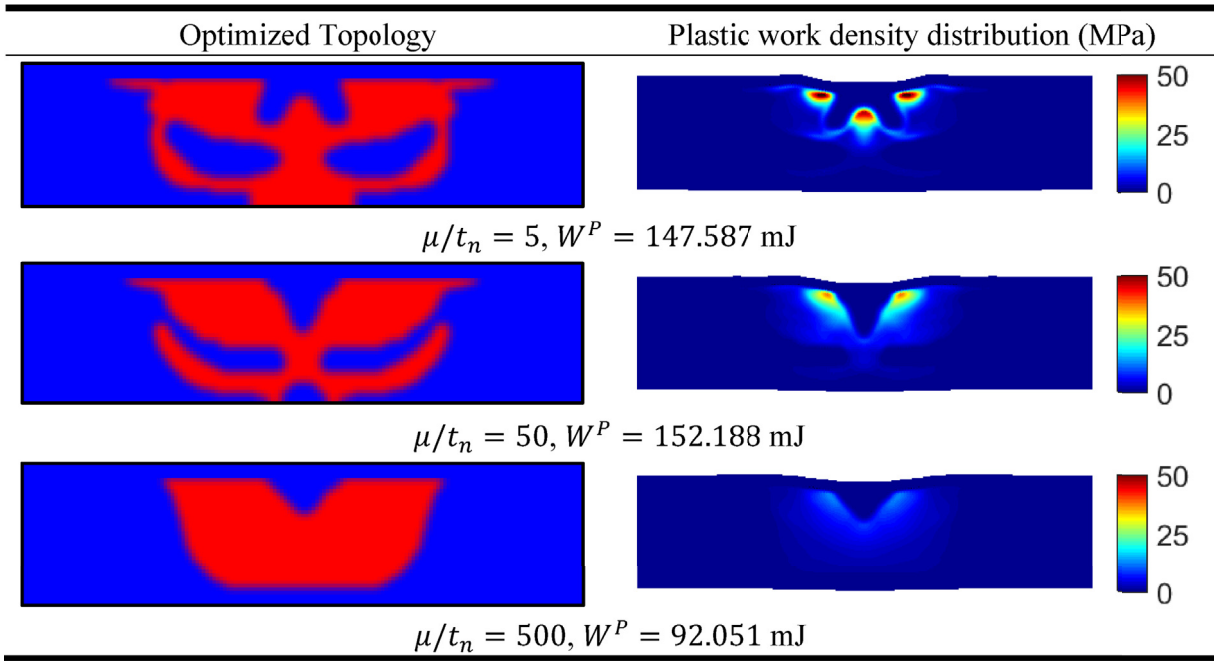

Fig. 13. Optimized topologies and distributions of plastic work density in deformed configuration for clamped beam problem under dynamic analysis with volume fraction $V_f = 0.3$ and different viscoplastic rate effects.

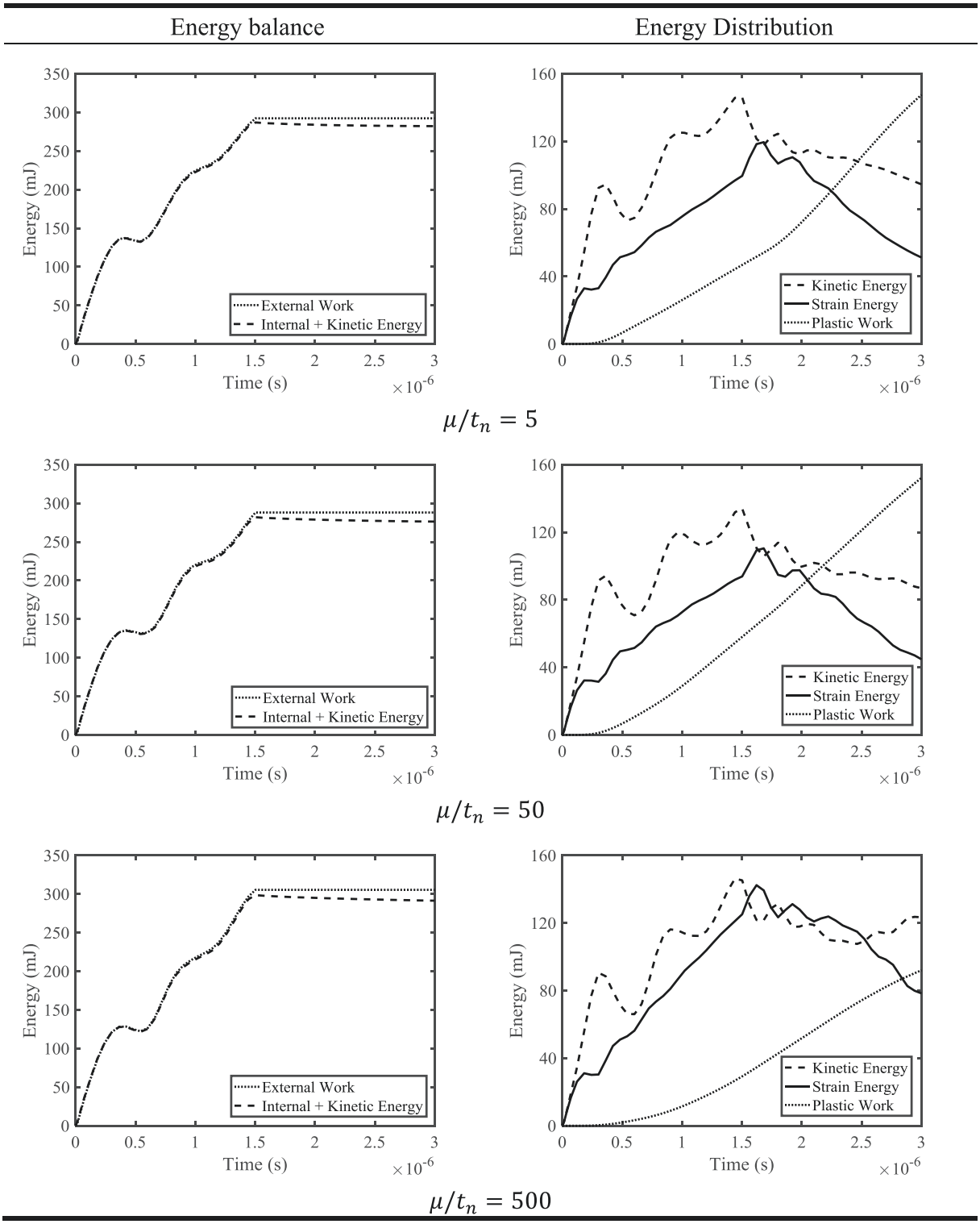

Fig. 15. Energy balance and distribution for optimized topologies obtained using dynamic analysis with volume fraction $V_f = 0.3$ and different viscoplastic rate effects.

damping. The energy distribution reveals that after the point when the applied displacement ceases to increase ($t = 1.5 \times 10^{-6}$ s), the kinetic and strain energies begin to drop. This is because there is no more energy entering the system (as seen by the plateaued external work) while the propagating shock wave continues to cause energy to be dissipated as plastic work (as seen by the increasing plastic work after this point).

With the behavior of this problem better understood, optimization is now carried out under quasi-static and dynamic analysis with the prescribed displacement $\overline{u}$ kept at 0.25 mm and rate effects suppressed by setting the rate sensitivity parameter $\vartheta = 0$. A volume fraction $V_f = 0.3$ of the energy dissipating elasto-viscoplastic phase is prescribed. The optimized topologies obtained are shown in Fig. 8 and it can be seen that

they are vastly different, reflecting the different physics being modeled. In the quasi-static case, a load path develops as the material carries stress resulting from the displacement applied at the center of the domain to the supports at the edges of the domain. When inertia effects are considered, the stresses resulting from the applied displacement propagate through the material in the form of a shock wave, since the time period considered during analysis is not long enough to allow the load path to fully develop. As the optimized topologies evolve so as to place the limited energy dissipating elasto-viscoplastic phase in regions where stress is high, they are very different.

This is also reflected in the distributions of plastic work density within the deformed configurations of the optimized topologies shown at the end of the analysis (i.e. at $t = 3 \times 10^{-6}$ s) in Fig. 9. In the topology obtained under quasi-static analysis, almost the entire volume of the elasto-viscoplastic phase has a similar density of plastic work, whereas in the topology obtained under dynamic analysis, the plastic work density is concentrated closer to where the propagating shock wave enters the domain. However, the total amount of energy dissipated as plastic work is much greater in the dynamic case since more total energy enters the system as external work to overcome inertia effects and reach the prescribed displacement.

The total external work and sum of the internal and kinetic energies are shown in Fig. 10 for the optimized topology obtained under dynamic loading. Comparison with Fig. 7 reveals that the total external work increases as more work is needed to obtain the same prescribed displacement when 70% of the domain now contains the stiffer hyperelastic phase. Also shown in Fig. 10 is the distribution into kinetic energy, strain energy and plastic work, where it can be seen that by the end of the time period considered during analysis, the plastic work is greater than both the kinetic and strain energies. In fact, for this optimized topology the ratio of the plastic work to the external work at the end of the analysis time period is 0.422, meaning that 42.2% of the total energy entering the system is dissipated as plastic work. When the entire volume of the domain excluding the buffer layer consists of the energy dissipating elasto-viscoplastic phase (82.5% of the domain), only 32.0% of the energy is dissipated as plastic work. Thus, using a volume of energy dissipating elasto-viscoplastic phase equal to only 30% of the domain volume and combining this in an optimized way with a stiffer hyperelastic phase leads to an increase of more than 12% in terms of the energy that can be dissipated, as comparted to using a volume of elasto-viscoplastic phase equal to 82.5% of the domain volume.

4.3. Rate effects

Next, the influence of rate effects on optimized topologies is investigated by setting the rate sensitivity parameter $\vartheta = 1$ and considering different ratios between the viscosity parameter and total deformation time, i.e. $\mu / t_n = 5$, 50, and 500. The optimized topologies obtained under quasi-static analysis are shown in Fig. 11 along with plastic work density distributions in the deformed configuration at the end of the analysis and the total plastic work W^P. It can be seen that distinct topologies are obtained for each value of μ / t_n. Additionally, convergence curves for these topologies are presented in Fig. 12 along with the convergence curve for the topology obtained without rate effects (Fig. 8a). It can be seen that convergence is smooth for all cases.

As rate effects become more prominent the stress needed to initiate yielding increases, resulting in a more uniform distribution of stress throughout the domain but reducing the plastic flow. Moreover, the more even distribution of higher stress leads to an increase in the total plastic work even as the plastic flow is reduced. These phenomena are exploited in the way the hard hyperelastic phase is combined with the soft energy dissipating elasto-viscoplastic phase in optimized topologies. For instance, when $\mu / t_n = 5$ it is more efficient to use thinner regions of the elasto-viscoplastic phase so as to cause localization of plastic yielding due to the high stresses transferred between regions of the surrounding hard hyperelastic phase. In fact, the volume constraint is not even active for this case, which only utilizes 19.0% of the energy dissipating elasto-viscoplastic phase. The same explanation can be given for the topology obtained without rate effects (Fig. 8), but the lower yield stress for that case allows yielding in a larger volume of this phase near the top of the domain where the displacement is applied. When rate effects are increased, however, decreasing plastic flow necessitates inducing yielding in a greater volume of the energy dissipating elasto-viscoplastic phase to increase the plastic work. Finally, rate effects are increased to a

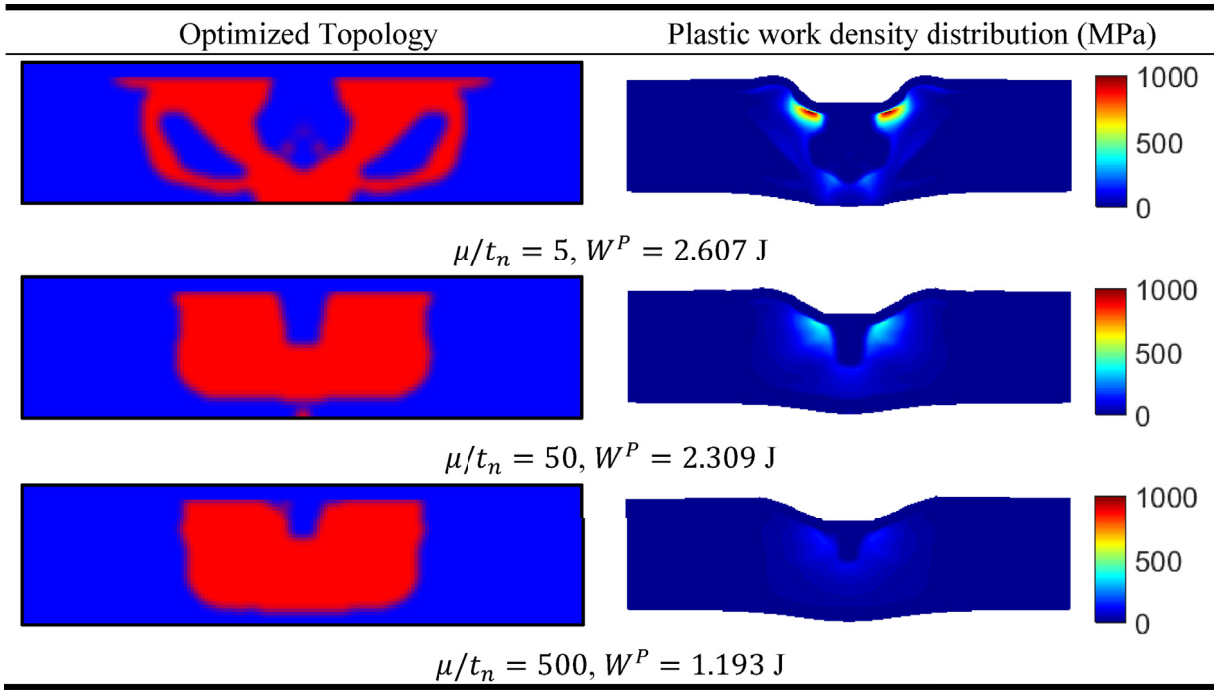

Fig. 16. Optimized topologies and distributions of plastic work density in deformed configuration for clamped beam problem under dynamic analysis with volume fraction $V_f = 0.3$ and different viscoplastic rate effects when $\bar{u}$ is increased to 1 mm.

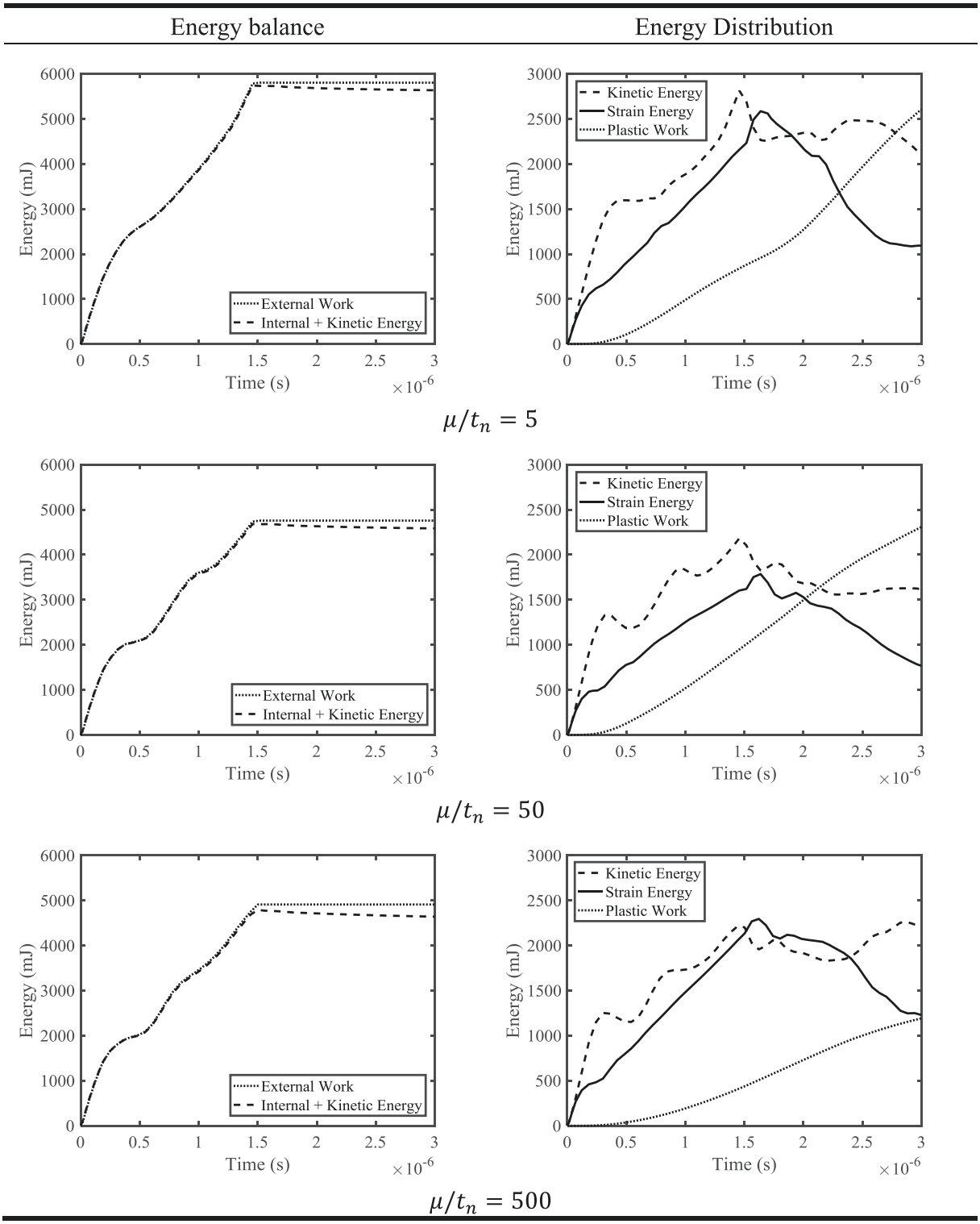

Fig. 17. Energy balance and distribution for optimized topologies obtained using dynamic analysis with volume fraction $V_f = 0.3$ and different viscoplastic rate effects when $\bar{u}$ is increased to 1 mm.

point where even the higher stresses cannot make up for the lack of plastic flow and the plastic work drops, as when $\mu/t_n =$ 500. These trends can be seen in the plastic work density distributions of Fig. 11.

Fig. 13 shows the optimized topologies obtained under dynamic analysis along with the plastic work density distributions in the deformed configuration and the total plastic work W^p. Additionally, Fig. 14 shows convergence curves for the optimized topologies obtained under dynamic analysis with different rate effects, and it can be seen that convergence progresses smoothly. These results reflect similar trends as in the quasi-static case. That is, with lower rate effects it is more efficient to arrange the elasto-viscoplastic phase so that plastic yielding is more localized, as seen in the optimized topologies and plastic work density distributions when no rate effects are considered and when $\mu/t_n = 5$. As rate effects become more prominent, it is no longer efficient to rely on

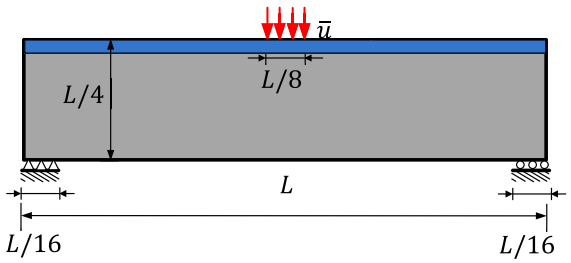

Fig. 18. Simply supported beam problem configuration.

localizing regions of this phase since there will be less resulting plastic flow. Instead, it is best to use large continuous regions of the energy dissipating elasto-viscoplastic phase since yielding can occur more uniformly. When rate effects are very high ($\mu/t_n = 500$) a drop in the total plastic work is unavoidable as the plastic flow decreases significantly. Again, the plastic work density distributions bear out these trends.

In Fig. 15 the total external work and sum of the internal and kinetic energies is shown along with the distribution of energy into kinetic energy, strain energy and plastic work for all three cases of rate effects under dynamic analysis. It can be seen that the external work is similar when $\mu/t_n = 5$ and $\mu/t_n = 50$, but is increased when $\mu/t_n = 500$ due to the fact that there is less plastic flow so more work must be done to reach the prescribed displacement. Indeed, when $\mu/t_n = 5$ and $\mu/t_n = 50$, the percentage of the total energy which is dissipated as plastic work is 50.5% and 52.8%, respectively When $\mu/t_n = 500$, however, only 30.1% of the energy which enters the system is dissipated as plastic work. Again, this shows how high rate effects can be detrimental.

Finally, Fig. 16 shows the optimized topologies along with the plastic work density distributions in the deformed configuration and the total plastic work W^P obtained under dynamic analysis when the prescribed displacement $\bar{u}$ is increased to 1 mm (20% of the domain height) and rate effects are considered. It can be seen that similar trends are followed in the optimized topologies as the rate is increased, but that an increasing rate leads to decreasing plastic work even when $\mu/t_n = 50$. Hence, the larger applied displacement leads to higher stresses which exacerbate material rate effects. This can be seen also in the plastic work density distributions, where the values drop significantly as rates are increased and there is less distortion at the top of the domain. The total external work and sum of the internal and kinetic energies is shown in Fig. 17 along with the distribution into kinetic energy, strain energy and plastic work for these topologies. It can be seen that when the prescribed displacement $\bar{u}$ is increased to 1, the total energy entering the system is highest for $\mu/t_n = 5$, whereas the total energy entering the system is highest for $\mu/t_n = 500$ when $\bar{u}$ is 0.25 mm. In terms of the percentage of total energy dissipated through plastic work, the optimized topologies obtained when $\bar{u}$ is increased to 1 mm follow the same trend as when $\bar{u}$ is 0.25 mm. That is, this percentage is 44.9% for $\mu/t_n = 5$, 48.5% when $\mu/t_n = 50$ and 24.3% when $\mu/t_n = 500$.

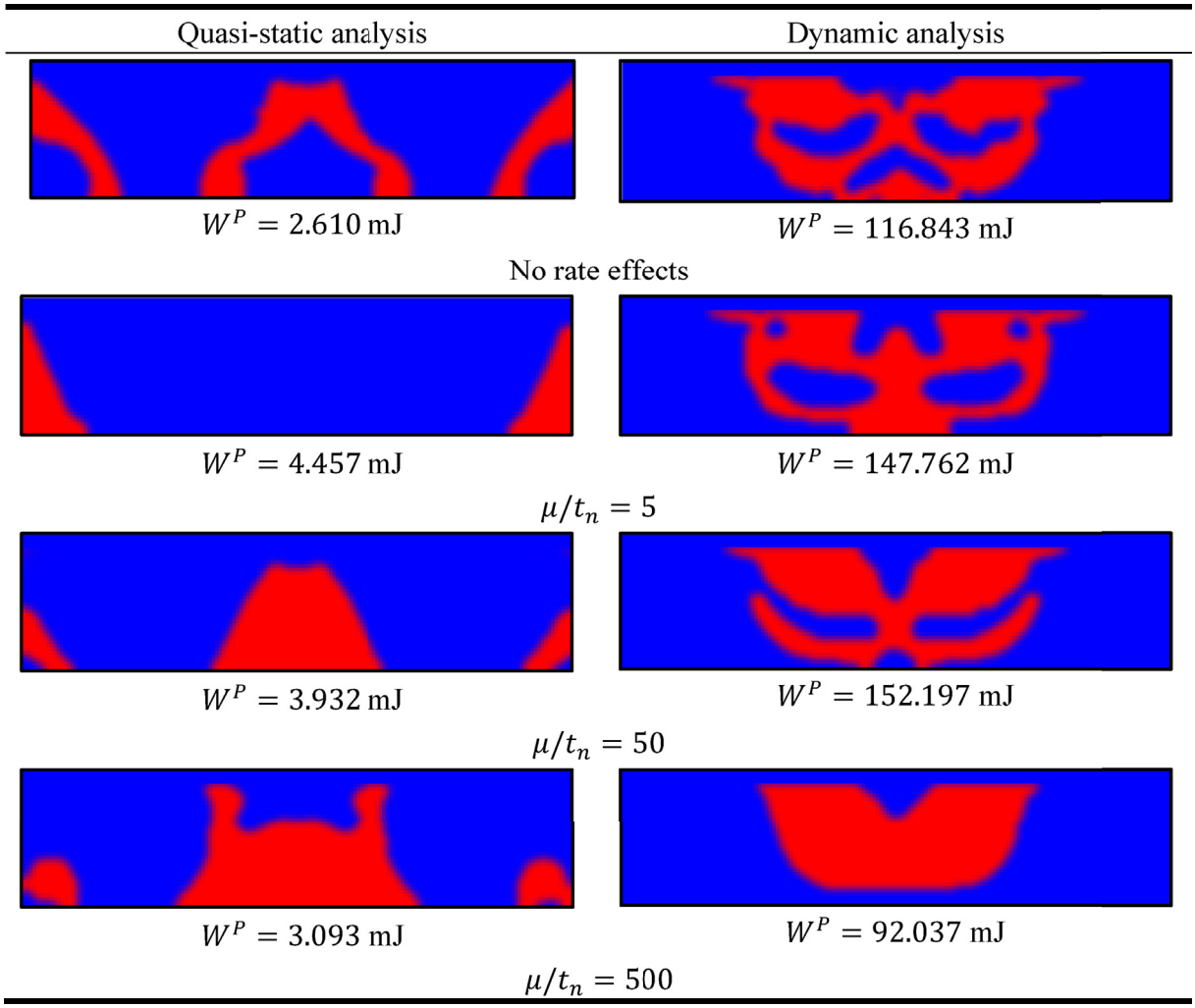

Fig. 19. Optimized topologies for simply supported beam problem under quasi-static analysis and dynamic analysis with volume fraction $V_f = 0.3$ and different viscoplastic rate effects.

4.4. Boundary conditions

The final example concerns the influence of boundary conditions on optimized topologies. To explore this, the simply supported beam problem shown in Fig. 18 is considered. This problem consists of the same domain as the clamped beam problem (Fig. 5) but with a change in boundary conditions. The prescribed displacement $\overline{u} = 0.25$ mm is applied as described in Section 4.2 and the volume fraction of elasto-viscoplastic phase is again set to $V_f = 0.3$. Optimization is carried out using both quasi-static and dynamic analysis for cases considering no rate effects ($\vartheta = 0$) and rate effects with $\mu / t_n = 5$, 50, and 500.

Fig. 19 shows the optimized topologies for each case and also reports the total plastic work W^p. Comparison with Figs. 8 and 11 reveals that the topologies obtained under quasi-static analysis differ significantly from those obtained for the clamped beam problem, which should be expected due to the change in boundary conditions. However, the topologies obtained under dynamic analysis closely resemble those in Figs. 8 and 13, despite this change in boundary conditions. As discussed in Section 4.2, stresses propagate through the domain as a shock wave when inertia effects are considered and do not reach the supports within the time period used for analysis. Hence, if inertia effects are considered within a short enough time period, the boundary conditions do not influence optimized topologies.

5. Conclusions

This study develops a topology optimization formulation for maximizing energy dissipation while considering the phenomena of material rate effects, inertia effects, and large deformations. Simulation of finite deformation dynamics with elasto-viscoplastic material behavior necessitates the use of sophisticated numerical techniques, which are directly accommodated within the adjoint sensitivity formulation so that design updates are driven directly by the simulated physics. A bi-material interpolation scheme is developed within the density-based design parameterization and used to obtain optimized distributions of a hard hyperelastic phase providing stiffness and a soft elasto-viscoplastic phase providing energy dissipation capacity. Optimized designs are shown to exploit the physics of these two phases under both quasi-static and dynamic analyses, resulting in discrete topologies. A much higher percentage of the total energy can be dissipated as plastic work when the energy dissipating phase is combined in an optimized way with a stiffness providing phase than when the energy dissipating phase is considered alone. Moreover, isolating the influence of material rate effects from inertia effects reveals that optimized designs exploit similar phenomena with or without inertia effects. These results provide insight into how to lay out material phases so as to increase energy dissipation for applications such as impact mitigation where large deformations occur along with prominent inertia and material rate effects.

The bi-material interpolation scheme developed in this study can be extended to consider different phenomenological constitutive relations. For example, to delay material failure in optimized designs coupled elasto-viscoplastic damage models can be considered, as described in Refs. [17,18]. Additionally, solid-void and multimaterial topology optimization can be carried out by treating voids as an additional material phase modeled with the ersatz material (fictitious domain) approach. However, this approach presents additional challenges regarding excessive mesh distortions [45] and large plastic strains in intermediate density elements. This work is currently being carried out by the authors.

Acknowledgements

The presented work is supported in part by the US National Science Foundation through Grant CMMI-1762277. Any opinions, findings, conclusions, and recommendations expressed in this paper are those of the authors and do not necessarily reflect the views of the sponsors.

Appendix C. Supplementary data

Supplementary data to this article can be found online at https://doi.org/10.1016/j.finel.2019.06.003.

Appendix A. Exponential Return Mapping Algorithm

This appendix presents the exponential return mapping algorithm used to numerically implement the viscoplastic material model discussed in Section 2.2. For time step $m+1$ at integration point r of element e, given information includes the current and previous step deformation (characterized by $\overline{\boldsymbol{F}}_{e_r}^{m+1}$ and $\overline{\boldsymbol{F}}_{e_r}^{m}$) and the previous step internal variables ($\mathcal{J}_{e_r}^{m} = \{\boldsymbol{b}_{e_r}^{e^m}, \alpha_{e_r}^{m}\}$). The purpose of the constitutive algorithm is to calculate the current step stress $\overline{\boldsymbol{P}}_{e_r}^{m+1}$, internal variables $\mathcal{J}_{e_r}^{m+1}$ and the consistent tangent modulus $\overline{\mathbb{A}}_T$ needed to evaluate the tangent matrix in Eq. (7). The exponential return mapping algorithm detailed in this appendix is presented with the superscript removed from variables at the current time step $m+1$ and no reference made to element or integration point number. Likewise, the bar is removed from any of the F-bar quantities so that the algorithm is presented independently from the type of element used.

Making use of the relations for the plastic distortion-rate tensor $\boldsymbol{L}^p = \dot{\boldsymbol{F}}^p.\boldsymbol{F}^{p-1} = \boldsymbol{F}^{e-1}.\boldsymbol{l}^p.\boldsymbol{F}^e$ and the polar decomposition $\boldsymbol{F}^e = \boldsymbol{V}^e.\boldsymbol{R}^e$ as well as Eq. (17), the rate equation for the plastic part of the deformation gradient $\boldsymbol{F}^p$ can be written as

$$\dot{\boldsymbol{F}}^p = \boldsymbol{R}^{e\,T}.\boldsymbol{A}.\boldsymbol{R}^e.\boldsymbol{F}^p \tag{A.1}$$

This rate equation is numerically approximated using the exponential mapping integrator, giving

$$\boldsymbol{F}^p = \exp\left[\Delta t \boldsymbol{R}^{e\,T}.\boldsymbol{A}.\boldsymbol{R}^e\right].\boldsymbol{F}_n^p = \boldsymbol{R}^{e\,T}.\exp[\Delta t \boldsymbol{A}].\boldsymbol{R}^e.\boldsymbol{F}_n^p \tag{A.2}$$

The exponential map integrator is used as it preserves the incompressibility of plastic flow, i.e. it ensures that $\det \boldsymbol{F}^p = 1$. Using Eq. (A.2) along with the definitions $\boldsymbol{F}^e = \boldsymbol{F}.\boldsymbol{F}^{p\,-1}$ and $\boldsymbol{b}^e = \boldsymbol{V}^{e2}$ results in the following discrete flow rule for $\boldsymbol{b}^e$

$$\boldsymbol{b}^e = \exp[-2\Delta t \boldsymbol{A}].\boldsymbol{F}.\boldsymbol{F}_n^{-1}.\boldsymbol{b}_n^e.\boldsymbol{F}_n^{-T}.\boldsymbol{F}^T = \boldsymbol{b}^{e,tr}.\exp[-2\Delta t \boldsymbol{A}] \tag{A.3}$$

where the trial elastic left Cauchy-Green deformation tensor is defined as $\boldsymbol{b}^{e,tr} = \Delta \boldsymbol{F}.\boldsymbol{b}_n^e.\Delta \boldsymbol{F}^T$ with $\Delta \boldsymbol{F} = \boldsymbol{F}.\boldsymbol{F}_n^{-1}$ and can be seen to depend on the given previous step information $\boldsymbol{b}_n^e$ and $\boldsymbol{F}_n$ and current step information $\boldsymbol{F}$. The discrete flow rule Eq. (A.3) can be greatly simplified by considering its evaluation in the space spanned by the elastic left principal directions $\boldsymbol{l}_a^e, a = 1, 2, 3$. In this space,

$$\begin{aligned} \boldsymbol{b}^e &= \sum_a^3 \lambda_a^{e\,2} \boldsymbol{l}_a^e \otimes \boldsymbol{l}_a^e \\ \boldsymbol{b}^{e,tr} &= \sum_a^3 \lambda_a^{e,tr\,2} \boldsymbol{l}_a^{e,tr} \otimes \boldsymbol{l}_a^{e,tr} \end{aligned} \tag{A.4}$$

Given the coaxiality between $\boldsymbol{b}^e$ and $\boldsymbol{\tau}$ resulting from the assumption of isotropy, together with the coaxiality between $\boldsymbol{b}^e$ and $\boldsymbol{A}$ resulting from the assumption of associativity, the principal directions $\boldsymbol{l}_a^e$ coincide with $\boldsymbol{l}_a^{e,tr}$. Thus, in principal space, Eq. (A.3) is

$$\lambda_a^{e^2} = \exp\left[-2\Delta\gamma\sqrt{\frac{3}{2}} n_a \right] \lambda_a^{e,tr^2}, \quad a = 1,\ 2,\ 3 \tag{A.5}$$

where n_a are the principal components of the flow vector $\boldsymbol{n}$. Taking the natural logarithm of this expression results finally in the discrete flow rule for the logarithmic elastic principal stretches $\varepsilon_a^e = \ln \lambda_a^e$, i.e.

$$\varepsilon_a^e = \varepsilon_a^{e,tr} - \Delta\gamma\sqrt{\frac{3}{2}} n_a, a = 1,\ 2,\ 3 \tag{A.6}$$

which can be seen to coincide with the discrete flow rule for the elastic strains in the small strain case [28].

Complementing the discrete flow rule in Eq. (A.6) with the discrete flow rule for the accumulated plastic strain α obtained by utilizing a backward Euler integration thus provides the necessary equations for carrying out the return mapping algorithm. The first step of this algorithm is the elastic trial step which is performed as follows

$$\begin{aligned} &\text{Given: } \boldsymbol{F}, \boldsymbol{b}^{e,tr} = \boldsymbol{F}.\boldsymbol{F}_n^{-1}.\boldsymbol{b}_n^e.\boldsymbol{F}_n^{-T}.\boldsymbol{F}^T,\ \alpha^{tr} = \alpha_m \\ &\text{Evaluate using the trial elastic principal stretch values in Eq.(13). Compute} \\ &\boldsymbol{s}^{tr} = \mathbb{P}_{dev}^s \boldsymbol{\tau}^{tr} \\ &q^{tr} = K^h \alpha^{tr} \\ &\varphi^{tr}(\boldsymbol{\tau}^{tr}, q^{tr}) = \sqrt{\frac{3}{2}} \|\boldsymbol{s}^{tr}\| - \left(\sigma_y + q^{tr}\right) \end{aligned} \tag{A.7}$$

with $\boldsymbol{\tau}^{tr} = \begin{bmatrix} \tau_1^{tr} & \tau_2^{tr} & \tau_3^{tr} \end{bmatrix}^T$, $\boldsymbol{s}^{tr} = \begin{bmatrix} s_1^{tr} & s_2^{tr} & s_3^{tr} \end{bmatrix}^T$, and $\|\boldsymbol{s}^{tr}\| = \sqrt{s_1^{tr\,2} + s_2^{tr\,2} + s_3^{tr\,2}}$. The matrix $\mathbb{P}_{dev}^s = \boldsymbol{I} - \mathbf{1}/3$ where $\mathbf{1}$ is a matrix whose entries are all 1.

If $\phi^{tr} \leq 0$ then the current step is an elastic step and the following elastic updates are made

$$\begin{aligned} &\boldsymbol{b}^e = \boldsymbol{b}^{etr}, \alpha = \alpha^{tr}, \boldsymbol{\tau} = \boldsymbol{\tau}^{tr} \\ &\mathbb{A}_T = \mathbb{A} \end{aligned} \tag{A.8}$$

where $\mathbb{A}$ is the matrix form of the tangent moduli tensor $\mathbb{A} = \partial^2\psi/\partial\boldsymbol{F}\partial\boldsymbol{F}$ for the strain energy function defined in Eq. (13).

Else, if $\phi^{tr} > 0$ then plastic flow is occurring in this step and the algorithm proceeds to Step 2, the viscoplastic return mapping step. In this step, the initial value problem defined by the flow rules given in Eq. (16) must be evaluated numerically. Making use of Eq. (A.6), the discrete update equations for the time step $\Delta t = t - t_m$ are

$$\begin{aligned} &\varepsilon_a^e = \varepsilon_a^{e,tr} - \Delta\gamma\sqrt{\frac{3}{2}} n_a, a = 1,2,3 \\ &\alpha = \alpha_m + \Delta\gamma \\ &\Delta\gamma = \frac{1}{\mu}\left[\left(\sqrt{\frac{3}{2}}\ \frac{\|s\|}{\zeta} \right)^{\frac{1}{\theta}} - 1 \right] \Delta t \\ &n_a = \frac{-s_a}{\boldsymbol{s}} \end{aligned} \tag{A.9}$$

Combining Eqn. (A.9)$_2$ and (A.9)$_3$ thus results in the nonlinear algebraic system

$$\boldsymbol{R} = \begin{bmatrix} \boldsymbol{R}_1 \\ R_2 \end{bmatrix} = \begin{bmatrix} \boldsymbol{\varepsilon}^e - \boldsymbol{\varepsilon}^{e^{tr}} + \Delta\gamma\sqrt{\frac{3}{2}}\boldsymbol{n} \\ \Delta\gamma - \frac{\Delta t}{\mu}\left[\left(\sqrt{\frac{3}{2}}\ \frac{\boldsymbol{s}}{\zeta(\Delta\gamma)} \right)^{\frac{1}{\theta}} - 1 \right] \end{bmatrix} = \begin{bmatrix} \mathbf{0} \\ \mathbf{0} \end{bmatrix} \tag{A.10}$$

which is solved for the unknowns $\boldsymbol{X} = \begin{bmatrix} \boldsymbol{\varepsilon}^e & \Delta\gamma \end{bmatrix}^T$ using the Newton-Raphson method with tangent matrix

$$\frac{d\boldsymbol{R}}{d\boldsymbol{X}} = \begin{bmatrix} \boldsymbol{I} + \dfrac{\Delta\gamma}{s}\sqrt{\dfrac{3}{2}}\left(\mathbb{P}^{s}_{dev} - \boldsymbol{n}\otimes\boldsymbol{n}\right)\boldsymbol{B} & \sqrt{\dfrac{3}{2}}\boldsymbol{n} \\ \left(\dfrac{\Delta t}{\mu\Delta\gamma + \Delta t}\right)^{\vartheta}\sqrt{\dfrac{3}{2}}\boldsymbol{n}^{T}\boldsymbol{B} & -\left(\sqrt{\dfrac{3}{2}}\left(\dfrac{\Delta t}{\mu\Delta\gamma + \Delta t}\right)^{\vartheta}\dfrac{\vartheta\mu\|\boldsymbol{s}\|}{\mu\Delta\gamma + \Delta t} + K^{h}\right) \end{bmatrix} \tag{A.11}$$

Here, $\boldsymbol{B}$ is a matrix containing the terms $\partial\tau_a/\partial\varepsilon^e_b, a, b = 1, 2, 3$. The converged values of ε^e_a are used to obtain the elastic principal stretches λ^e_a and by extension $\boldsymbol{b}^e$. The converged values τ_a are used to obtain $\boldsymbol{\tau}$ and the first Piola-Kirchhoff stress tensor is calculated as $\boldsymbol{P} = \boldsymbol{\tau}.\boldsymbol{F}^{-T}$. The algorithmic consistent tangent modulus $\mathbb{A}_T$ can then be calculated in component form as

$$\mathbb{A}_{ijkl} = J\mathrm{a}_{ipkr}F^{-1}_{jp}F^{-1}_{lr} \tag{A.12}$$

where the spatial moduli tensor a is given as

$$J\mathrm{a} = \frac{\partial\boldsymbol{\tau}}{\partial\boldsymbol{b}^{e,tr}} : \left(\boldsymbol{I}\boxtimes\boldsymbol{b}^{e,tr^{T}} + \boldsymbol{b}^{e,tr}\boxdot\boldsymbol{I}\right) - \boldsymbol{\tau}\boxdot\boldsymbol{I} \tag{A.13}$$

and the products $\boxtimes$ and $\boxdot$ between 2nd order tensors are defined as $(\boldsymbol{A}\boxtimes\boldsymbol{B})_{ijkl} = A_{ik}B_{jl}$ and $(\boldsymbol{A}\boxdot\boldsymbol{B})_{ijkl} = A_{il}B_{jk}$. The term $\partial\boldsymbol{\tau}/\partial\boldsymbol{b}^{e,tr}$ is computed in principal space using data from the constitutive Newton-Raphson routine as

$$\left[\frac{\partial\tau_a}{\partial b^{e,tr}_b}\right]_{a,b=1,2,3} = \boldsymbol{B}\boldsymbol{D}_{11}$$

with

$$\frac{d\boldsymbol{R}^{-1}}{d\boldsymbol{X}} = \begin{bmatrix} \boldsymbol{D}_{11} & \boldsymbol{D}_{12} \\ \boldsymbol{D}_{21} & \boldsymbol{D}_{22} \end{bmatrix} \tag{A.14}$$

and then brought to physical space for use in Eq. (A.13). This completes the exponential return mapping algorithm.

Appendix B. Derivatives for Sensitivity Analysis

Based on the definition of global and local state variables defined in Section 3.3, the derivatives needed for sensitivity analysis (Eq. (30)) are presented in this appendix. In the expressions below, use is made of the products $\boxtimes$ and $\boxdot$ between 2nd order tensors, defined in Appendix A as $(\boldsymbol{A}\boxtimes\boldsymbol{B})_{ijkl} = A_{ik}B_{jl}$ and $(\boldsymbol{A}\boxdot\boldsymbol{B})_{ijkl} = A_{il}B_{jk}$.

B.1: Derivatives of global constraints

The derivative of the global constraint $\boldsymbol{R}^k$ with respect to the element density variable vector $\boldsymbol{\rho}$ is

$$\frac{\partial\boldsymbol{R}^k}{\partial\boldsymbol{\rho}} = \begin{bmatrix} \dfrac{\partial\boldsymbol{R}^k_u}{\partial\boldsymbol{\rho}} \\ \dfrac{\partial\boldsymbol{R}^k_v}{\partial\boldsymbol{\rho}} \\ \dfrac{\partial\boldsymbol{R}^k_a}{\partial\boldsymbol{\rho}} \end{bmatrix} = \begin{bmatrix} \overset{n_{ele}}{\underset{e=1}{\mathcal{A}}}\left(\dfrac{\partial\tilde{\boldsymbol{F}}^{e^k}_{int}}{\partial\rho_e}\right) \\ \boldsymbol{0} \\ \boldsymbol{0} \end{bmatrix} \tag{B.1}$$

with

$$\begin{aligned} \frac{\partial\tilde{\boldsymbol{F}}^{e^k}_{int}}{\partial\rho_e} &= (1+\alpha)\frac{\partial\boldsymbol{F}^{e^k}_{int}}{\partial\rho_e} - \alpha\frac{\partial\boldsymbol{F}^{e^{k-1}}_{int}}{\partial\rho_e} + \frac{1}{\beta\Delta t^2}\frac{\partial\chi_\rho}{\partial\rho_e}\boldsymbol{M}_e\left(\boldsymbol{u}^k_e - \tilde{\boldsymbol{u}}^k_e\right) \\ \frac{\partial\boldsymbol{F}^{e^k}_{int}}{\partial\rho_e} &= \sum_{r=1}^{n_{ipt}} w_r r^{k^{a-1}}_{e_r}\boldsymbol{B}^T_{e_r}\frac{\partial\overline{\boldsymbol{P}}^k_{e_r}}{\partial\rho_e} \\ \frac{\partial\boldsymbol{F}^{e^{k-1}}_{int}}{\partial\rho_e} &= \sum_{r=1}^{n_{ipt}} w_r r^{k-1^{a-1}}_{e_r}\boldsymbol{B}^T_{e_r}\frac{\partial\overline{\boldsymbol{P}}^{k-1}_{e_r}}{\partial\rho_e} \\ \frac{\partial\overline{\boldsymbol{P}}^k_{e_r}}{\partial\rho_e} &= \frac{\overline{\boldsymbol{P}}^{k-1}_{e_r}}{\partial\rho_e} = \frac{\partial\chi_H}{\partial\rho_e}\overline{\boldsymbol{P}}^{HE^k}_{e_r} + \frac{\partial\chi_S}{\partial\rho_e}\overline{\boldsymbol{\tau}}^{VP^k}_{e_r}.\overline{\boldsymbol{F}}^{k^{-T}}_{e_r} \end{aligned} \tag{B.2}$$

Next, the derivative with respect to the global variables, $\partial\boldsymbol{R}^k/\partial\tilde{\boldsymbol{u}}^k$, is expanded as

$$\frac{\partial \boldsymbol{R}^k}{\partial \widehat{\boldsymbol{u}}^k}=\begin{bmatrix} \frac{\partial \boldsymbol{R}_u^k}{\partial \boldsymbol{u}^k} & \frac{\partial \boldsymbol{R}_u^k}{\partial \boldsymbol{v}^k} & \frac{\partial \boldsymbol{R}_u^k}{\partial \boldsymbol{a}^k} \\ \frac{\partial \boldsymbol{R}_v^k}{\partial \boldsymbol{u}^k} & \frac{\partial \boldsymbol{R}_v^k}{\partial \boldsymbol{v}^k} & \frac{\partial \boldsymbol{R}_v^k}{\partial \boldsymbol{a}^k} \\ \frac{\partial \boldsymbol{R}_a^k}{\partial \boldsymbol{u}^k} & \frac{\partial \boldsymbol{R}_a^k}{\partial \boldsymbol{v}^k} & \frac{\partial \boldsymbol{R}_a^k}{\partial \boldsymbol{a}^k} \end{bmatrix} = \begin{bmatrix} \overset{n_{ele}}{\mathcal{A}}_{e=1}\left(\frac{\partial \tilde{\boldsymbol{F}}_{int}^{e^k}}{\partial \boldsymbol{u}_e^k}\right) & \boldsymbol{0} & \boldsymbol{0} \\ -\frac{\gamma}{\beta\Delta t}\boldsymbol{I} & \boldsymbol{I} & \boldsymbol{0} \\ -\frac{1}{\beta\Delta t^2}\boldsymbol{I} & \boldsymbol{0} & \boldsymbol{I} \end{bmatrix} \tag{B.3}$$

where $\boldsymbol{I}$ is the identity matrix of appropriate size and

$$\frac{\partial \tilde{\boldsymbol{F}}_{int}^{e^k}}{\partial \boldsymbol{u}_e^k}=(1+\alpha)\frac{\partial \boldsymbol{F}_{int}^{e^k}}{\partial \boldsymbol{u}_e^k}+\frac{\chi_\rho}{\beta\Delta t^2}\boldsymbol{M}_e$$

with

$$\begin{aligned} \frac{\partial \boldsymbol{F}_{int}^{e^k}}{\partial \boldsymbol{u}_e^k} &= \sum_{r=1}^{n_{ipt}} w_r r_{e_r}^{k^{a-1}} \boldsymbol{B}_{e_r}^T \frac{\partial \overline{\boldsymbol{P}}_{e_r}^k}{\partial \boldsymbol{u}_e^k} + (a-1)\sum_{r=1}^{n_{ipt}} w_r r_{e_r}^{k^{a-2}} \boldsymbol{B}_{e_r}^T \overline{\boldsymbol{P}}_{e_r}^k \otimes \frac{\partial r_{e_r}^k}{\partial \boldsymbol{u}_e^k} \\ \frac{\partial \overline{\boldsymbol{P}}_{e_r}^k}{\partial \boldsymbol{u}_e^k} &= \left(\chi_H \overline{\mathbb{A}}_{e_r}^{HE^k} - \chi_S \overline{\boldsymbol{P}}_{e_r}^{VP^k} \boxdot \overline{\boldsymbol{F}}_{e_r}^{k^{-1}}\right) : \frac{\partial \overline{\boldsymbol{F}}_{e_r}^k}{\partial \boldsymbol{u}_e^k} \\ \frac{\partial r_{e_r}^k}{\partial \boldsymbol{u}_e^k} &= r_{e_r}^k \left(\boldsymbol{F}_{0_{e_r}}^{k^{-T}} : \frac{\partial \boldsymbol{F}_{0_{e_r}}^k}{\partial \boldsymbol{u}_e^k} - \boldsymbol{F}_{e_r}^{k^{-T}} : \frac{\partial \boldsymbol{F}_{e_r}^k}{\partial \boldsymbol{u}_e^k}\right) \end{aligned} \tag{B.4}$$

Expanding the derivative $\partial \boldsymbol{R}^k / \partial \widehat{\boldsymbol{u}}^{k-1}$ then gives

$$\frac{\partial \boldsymbol{R}^k}{\partial \widehat{\boldsymbol{u}}^{k-1}}=\begin{bmatrix} \frac{\partial \boldsymbol{R}_u^k}{\partial \boldsymbol{u}^{k-1}} & \frac{\partial \boldsymbol{R}_u^k}{\partial \boldsymbol{v}^{k-1}} & \frac{\partial \boldsymbol{R}_u^k}{\partial \boldsymbol{a}^{k-1}} \\ \frac{\partial \boldsymbol{R}_v^k}{\partial \boldsymbol{u}^{k-1}} & \frac{\partial \boldsymbol{R}_v^k}{\partial \boldsymbol{v}^{k-1}} & \frac{\partial \boldsymbol{R}_v^k}{\partial \boldsymbol{a}^{k-1}} \\ \frac{\partial \boldsymbol{R}_a^k}{\partial \boldsymbol{u}^{k-1}} & \frac{\partial \boldsymbol{R}_a^k}{\partial \boldsymbol{v}^{k-1}} & \frac{\partial \boldsymbol{R}_a^k}{\partial \boldsymbol{a}^{k-1}} \end{bmatrix} == \begin{bmatrix} \overset{n_{ele}}{\mathcal{A}}_{e=1}\left(\frac{\partial \tilde{\boldsymbol{F}}_{int}^{e^k}}{\partial \boldsymbol{u}_e^{k-1}}\right) & \overset{n_{ele}}{\mathcal{A}}_{e=1}\left(\frac{\partial \tilde{\boldsymbol{F}}_{int}^{e^k}}{\partial \boldsymbol{v}_e^{k-1}}\right) & \overset{n_{ele}}{\mathcal{A}}_{e=1}\left(\frac{\partial \tilde{\boldsymbol{F}}_{int}^{e^k}}{\partial \boldsymbol{a}_e^{k-1}}\right) \\ \frac{\gamma}{\beta\Delta t}\boldsymbol{I} & \left(\frac{\gamma}{\beta}-1\right)\boldsymbol{I} & \left(\frac{\Delta t\gamma}{2\beta}(1-2\beta)-(1-\gamma)\Delta t\right)\boldsymbol{I} \\ \frac{1}{\beta\Delta t^2}\boldsymbol{I} & \frac{1}{\beta\Delta t}\boldsymbol{I} & \frac{1}{2\beta}(1-2\beta)\boldsymbol{I} \end{bmatrix} \tag{B.5}$$

and the derivatives of $\tilde{\boldsymbol{F}}_{int}^{e^k}$ are

$$\begin{aligned} \frac{\partial \tilde{\boldsymbol{F}}_{int}^{e^k}}{\partial \boldsymbol{u}_e^{k-1}} &= -\alpha\frac{\partial \boldsymbol{F}_{int}^{e^{k-1}}}{\partial \boldsymbol{u}_e^{k-1}} - \frac{\chi_\rho}{\beta\Delta t^2}\boldsymbol{M}_e \\ \frac{\partial \tilde{\boldsymbol{F}}_{int}^{e^k}}{\partial \boldsymbol{v}_e^{k-1}} &= -\frac{\chi_\rho}{\beta\Delta t}\boldsymbol{M}_e \\ \frac{\partial \tilde{\boldsymbol{F}}_{int}^{e^k}}{\partial \boldsymbol{a}_e^{k-1}} &= -\frac{\chi_\rho(1-2\beta)}{2\beta}\boldsymbol{M}_e \end{aligned} \tag{B.6}$$

with

$$\begin{aligned} \frac{\partial \boldsymbol{F}_{int}^{e^{k-1}}}{\partial \boldsymbol{u}_e^{k-1}} &= \sum_{r=1}^{n_{ipt}} w_r r_{e_r}^{k-1^{a-1}} \boldsymbol{B}_{e_r}^T \frac{\partial \overline{\boldsymbol{P}}_{e_r}^{k-1}}{\partial \boldsymbol{u}_e^{k-1}} + (a-1)\sum_{r=1}^{n_{ipt}} w_r r_{e_r}^{k-1^{a-2}} \boldsymbol{B}_{e_r}^T \overline{\boldsymbol{P}}_{e_r}^{k-1} \otimes \frac{\partial r_{e_r}^{k-1}}{\partial \boldsymbol{u}_e^{k-1}} \\ \frac{\partial \overline{\boldsymbol{P}}_{e_r}^{k-1}}{\partial \boldsymbol{u}_e^{k-1}} &= \left(\chi_H \overline{\mathbb{A}}_{e_r}^{HE^{k-1}} - \chi_S \overline{\boldsymbol{P}}_{e_r}^{VP^{k-1}} \boxdot \overline{\boldsymbol{F}}_{e_r}^{k-1^{-1}}\right) : \frac{\partial \overline{\boldsymbol{F}}_{e_r}^{k-1}}{\partial \boldsymbol{u}_e^{k-1}} \\ \frac{\partial r_{e_r}^{k-1}}{\partial \boldsymbol{u}_e^{k-1}} &= r_{e_r}^{k-1} \left(\boldsymbol{F}_{0_{e_r}}^{k-1^{-T}} : \frac{\partial \boldsymbol{F}_{0_{e_r}}^{k-1}}{\partial \boldsymbol{u}_e^{k-1}} - \boldsymbol{F}_{e_r}^{k-1^{-T}} : \frac{\partial \boldsymbol{F}_{e_r}^{k-1}}{\partial \boldsymbol{u}_e^{k-1}}\right) \end{aligned} \tag{B.7}$$

For the derivatives with respect to the local variables $\boldsymbol{c}$, the term $\partial \boldsymbol{R}^k / \partial \boldsymbol{c}^k$ is expanded as

$$\begin{bmatrix} \frac{\partial \boldsymbol{R}_u^k}{\partial \boldsymbol{c}^k} \\ \frac{\partial \boldsymbol{R}_v^k}{\partial \boldsymbol{c}^k} \\ \frac{\partial \boldsymbol{R}_a^k}{\partial \boldsymbol{c}^k} \end{bmatrix} = \begin{bmatrix} \overset{n_{ele}}{\mathcal{A}}_{e=1}\left(\frac{\partial \tilde{\boldsymbol{F}}_{int}^{e^k}}{\partial \boldsymbol{c}^k}\right) \\ \boldsymbol{0} \\ \boldsymbol{0} \end{bmatrix} \tag{B.8}$$

with

$$\frac{\partial \tilde{\boldsymbol{F}}_{int}^{e^k}}{\partial \boldsymbol{c}^k} = (1+\alpha)\begin{bmatrix} \frac{\partial \boldsymbol{F}_{int}^{e^k}}{\partial \boldsymbol{c}_1^k} & \cdots & \frac{\partial \boldsymbol{F}_{int}^{e^k}}{\partial \boldsymbol{c}_{n_{ele}}^k} \end{bmatrix}$$

$$\frac{\partial \boldsymbol{F}_{int}^{e^k}}{\partial \boldsymbol{c}_e^k} = \begin{bmatrix} \frac{\partial \boldsymbol{F}_{int}^{e^k}}{\partial \boldsymbol{c}_{e_1}^k} & \frac{\partial \boldsymbol{F}_{int}^{e^k}}{\partial \boldsymbol{c}_{e_2}^k} & \frac{\partial \boldsymbol{F}_{int}^{e^k}}{\partial \boldsymbol{c}_{e_3}^k} & \frac{\partial \boldsymbol{F}_{int}^{e^k}}{\partial \boldsymbol{c}_{e_4}^k} \end{bmatrix} \tag{B.9}$$

The derivatives $\partial \boldsymbol{F}_{int}^{e^k} / \partial \boldsymbol{c}_{e_r}^k$ are

$$\frac{\partial \boldsymbol{F}_{int}^{e^k}}{\partial \boldsymbol{c}_{e_r}^k} = \begin{bmatrix} w_r r_{e_r}^{k^{a-1}} \boldsymbol{B}_{e_r}^T \frac{\partial \overline{\boldsymbol{P}}_{e_r}^k}{\partial \boldsymbol{b}_{e_r}^{e^k}} & \boldsymbol{0} & \boldsymbol{0} \end{bmatrix}^T \tag{B.10}$$

with

$$\frac{\partial \overline{\boldsymbol{P}}_{e_r}^k}{\partial \boldsymbol{b}_{e_r}^{e^k}} = \frac{\partial \left(\chi_S \overline{\boldsymbol{\tau}}_{e_r}^{VP^k} . \overline{\boldsymbol{F}}_{e_r}^{k^{-T}} \right)}{\partial \boldsymbol{b}_{e_r}^{e^k}}$$

Finally, the term $\partial \boldsymbol{R}^k / \partial \boldsymbol{c}^{k-1}$ has the same form as in Eqn. (B.8) but with

$$\frac{\partial \tilde{\boldsymbol{F}}_{int}^{e^{k-1}}}{\partial \boldsymbol{c}^{k-1}} = -\alpha \begin{bmatrix} \frac{\partial \boldsymbol{F}_{int}^{e^{k-1}}}{\partial \boldsymbol{c}_1^{k-1}} & \cdots & \frac{\partial \boldsymbol{F}_{int}^{e^{k-1}}}{\partial \boldsymbol{c}_{n_{ele}}^{k-1}} \end{bmatrix}$$

$$\frac{\partial \boldsymbol{F}_{int}^{e^{k-1}}}{\partial \boldsymbol{c}_e^{k-1}} = \begin{bmatrix} \frac{\partial \boldsymbol{F}_{int}^{e^{k-1}}}{\partial \boldsymbol{c}_{e_1}^{k-1}} & \frac{\partial \boldsymbol{F}_{int}^{e^{k-1}}}{\partial \boldsymbol{c}_{e_2}^{k-1}} & \frac{\partial \boldsymbol{F}_{int}^{e^{k-1}}}{\partial \boldsymbol{c}_{e_3}^{k-1}} & \frac{\partial \boldsymbol{F}_{int}^{e^{k-1}}}{\partial \boldsymbol{c}_{e_4}^{k-1}} \end{bmatrix} \tag{B.11}$$

$$\frac{\partial \boldsymbol{F}_{int}^{e^{k-1}}}{\partial \boldsymbol{c}_{e_r}^{k-1}} = \begin{bmatrix} w_r r_{e_r}^{k-1^{a-1}} \boldsymbol{B}_{e_r}^T \frac{\partial \overline{\boldsymbol{P}}_{e_r}^{k-1}}{\partial \boldsymbol{b}_{e_r}^{e^{k-1}}} & \boldsymbol{0} & \boldsymbol{0} \end{bmatrix}^T$$

$$\frac{\partial \overline{\boldsymbol{P}}_{e_r}^{k-1}}{\partial \boldsymbol{b}_{e_r}^{e^{k-1}}} = \chi_S \frac{\partial \left(\overline{\boldsymbol{\tau}}_{e_r}^{VP^{k-1}} . \overline{\boldsymbol{F}}_{e_r}^{k-1^{-T}} \right)}{\partial \boldsymbol{b}_{e_r}^{e^{k-1}}}$$

In Eqn. (B.10) and (B.11), the terms $\partial \overline{\boldsymbol{P}}_{e_r}^k / \partial \boldsymbol{b}_{e_r}^{e^k}$ and $\partial \overline{\boldsymbol{P}}_{e_r}^{k-1} / \partial \boldsymbol{b}_{e_r}^{e^{k-1}}$ have the component form

$$\frac{\partial \tau_{ip} F_{pj}^{-T}}{\partial b_{kl}^e} = \frac{\partial \tau_{ip}}{\partial b_{kl}^e} F_{pj}^{-T} \tag{B.12}$$

and $\partial \overline{\boldsymbol{\tau}}^{VP} / \partial \boldsymbol{b}^e$ can be computed in the constitutive algorithm.

B.2: Derivatives of local constraints

The derivative of the local constraints $\boldsymbol{H}^k$ with respect to the element density variable vector $\boldsymbol{\rho}$ is given by the block diagonal matrix

$$\frac{\partial \boldsymbol{H}^k}{\partial \boldsymbol{\rho}} = \begin{bmatrix} \frac{\partial \boldsymbol{H}_1^k}{\partial \rho_1} & \boldsymbol{0} & \cdots & \boldsymbol{0} \\ \boldsymbol{0} & \frac{\partial \boldsymbol{H}_2^k}{\partial \rho_2} & \cdots & \boldsymbol{0} \\ \vdots & \vdots & \ddots & \vdots \\ \boldsymbol{0} & \boldsymbol{0} & \cdots & \frac{\partial \boldsymbol{H}_{n_{ele}}^k}{\partial \rho_{n_{ele}}} \end{bmatrix} \text{ with } \frac{\partial \boldsymbol{H}_e^k}{\partial \rho_e} = \begin{bmatrix} \frac{\partial \boldsymbol{H}_{e_1}^k}{\partial \rho_e} \\ \frac{\partial \boldsymbol{H}_{e_2}^k}{\partial \rho_e} \\ \frac{\partial \boldsymbol{H}_{e_3}^k}{\partial \rho_e} \\ \frac{\partial \boldsymbol{H}_{e_4}^k}{\partial \rho_e} \end{bmatrix} \tag{B.13}$$

and the entries $\partial \boldsymbol{H}_{e_r}^k / \partial \rho_e$ are only nonzero at a viscoplastic step, having the form

$$\frac{\partial \boldsymbol{H}^k_{e_r}}{\partial \rho_e} = \begin{bmatrix} \frac{\partial \boldsymbol{h}^k_{e_{r1}}}{\partial \rho_e} & 0 & \frac{\partial h^k_{e_{r3}}}{\partial \rho_e} \end{bmatrix}^T$$

$$\frac{\partial \boldsymbol{h}^k_{e_{r1}}}{\partial \rho_e} = -\boldsymbol{b}^{e,tr}_{e_r} . \frac{\partial \exp\left[-2\Delta t \boldsymbol{A}^k_{e_r}\right]}{\partial \rho_e} \tag{B.14}$$

$$\frac{\partial h^k_{e_{r3}}}{\partial \rho_e} = \sqrt{\frac{3}{2}} \left(\frac{\Delta t}{\mu \Delta \gamma^k_{e_r} + \Delta t} \right)^{\vartheta} \boldsymbol{n}^k_{e_r} : \left(\frac{\partial \chi_S}{\partial \rho_e} \boldsymbol{\tau}^{VP^k}_{e_r} \right)$$

The term $\partial \exp[-2\Delta t \boldsymbol{A}^k_{e_r}] / \partial \rho_e$ is computed in the principal space, where for each principal value the derivative is

$$\frac{\partial \exp\left[-2\Delta\gamma \sqrt{\frac{3}{2}} n_a \right]}{\partial \rho_e} = -2\Delta\gamma \sqrt{\frac{3}{2}} \exp\left[-2\Delta\gamma \sqrt{\frac{3}{2}} n_a \right] \frac{\partial n_a}{\partial \tau_a} \left(\frac{\partial \chi_S}{\partial \rho_e} \tau_a \right), a = 1, 2, 3 \tag{B.15}$$

The derivatives with respect to the global variables $\widehat{\boldsymbol{u}}$ are

$$\frac{\partial \boldsymbol{H}^k}{\partial \widehat{\boldsymbol{u}}^k} = \begin{bmatrix} \frac{\partial \boldsymbol{H}^k}{\partial \boldsymbol{u}^k} \\ \frac{\partial \boldsymbol{H}^k}{\partial \boldsymbol{v}^k} \\ \frac{\partial \boldsymbol{H}^k}{\partial \boldsymbol{a}^k} \end{bmatrix} = \begin{bmatrix} \frac{\partial \boldsymbol{H}^k}{\partial \boldsymbol{u}^k} \\ \boldsymbol{0} \\ \boldsymbol{0} \end{bmatrix} \text{ and } \frac{\partial \boldsymbol{H}^k}{\partial \widehat{\boldsymbol{u}}^{k-1}} = \begin{bmatrix} \frac{\partial \boldsymbol{H}^k}{\partial \boldsymbol{u}^{k-1}} \\ \frac{\partial \boldsymbol{H}^k}{\partial \boldsymbol{v}^{k-1}} \\ \frac{\partial \boldsymbol{H}^k}{\partial \boldsymbol{a}^{k-1}} \end{bmatrix} = \begin{bmatrix} \frac{\partial \boldsymbol{H}^k}{\partial \boldsymbol{u}^{k-1}} \\ \boldsymbol{0} \\ \boldsymbol{0} \end{bmatrix} \tag{B.16}$$

and the nonzero submatrix $\partial \boldsymbol{H}^k / \partial \boldsymbol{u}^k$ has the structure

$$\frac{\partial \boldsymbol{H}^k}{\partial \boldsymbol{u}^k} = \begin{bmatrix} \frac{\partial \boldsymbol{H}^k_1}{\partial \boldsymbol{u}^k} \\ \vdots \\ \frac{\partial \boldsymbol{H}^k_{n_{ele}}}{\partial \boldsymbol{u}^k} \end{bmatrix} \text{ with } \frac{\partial \boldsymbol{H}^k_j}{\partial \boldsymbol{u}^k} = \overset{n_{ele}}{\underset{e=1}{\mathcal{A}}} \left(\frac{\partial \boldsymbol{H}^k_j}{\partial \boldsymbol{u}^k_e} \right), j = 1, 2, \ldots, n_{ele} \tag{B.17}$$

Here, $\partial \boldsymbol{H}^k_j / \partial \boldsymbol{u}^k_e = \boldsymbol{0}$ if $j \neq e$. The nonzero entries, $\partial \boldsymbol{H}^k_e / \partial \boldsymbol{u}^k_e$, are

$$\frac{\partial \boldsymbol{H}^k_e}{\partial \boldsymbol{u}^k_e} = \begin{bmatrix} \frac{\partial \boldsymbol{H}^k_{e_1}}{\partial \boldsymbol{u}^k_e} & \frac{\partial \boldsymbol{H}^k_{e_2}}{\partial \boldsymbol{u}^k_e} & \frac{\partial \boldsymbol{H}^k_{e_3}}{\partial \boldsymbol{u}^k_e} & \frac{\partial \boldsymbol{H}^k_{e_4}}{\partial \boldsymbol{u}^k_e} \end{bmatrix}^T \tag{B.18}$$

with

$$\frac{\partial \boldsymbol{H}^k_{e_r}}{\partial \boldsymbol{u}^k_e} = \begin{bmatrix} -\frac{\partial \boldsymbol{b}^{e,tr}_{e_r}}{\partial \boldsymbol{u}^k_e} & 0 & 0 \end{bmatrix}^T$$

$$\frac{\partial \boldsymbol{b}^{e,tr}_{e_r}}{\partial \boldsymbol{u}^k_e} = \frac{\partial \boldsymbol{b}^{e,tr}_{e_r}}{\partial \overline{\boldsymbol{F}}^k_{e_r}} : \frac{\partial \overline{\boldsymbol{F}}^k_{e_r}}{\partial \boldsymbol{u}^k_e} \tag{B.19}$$

$$\frac{\partial \boldsymbol{b}^{e,tr}_{e_r}}{\partial \overline{\boldsymbol{F}}^k_{e_r}} = \boldsymbol{I} \boxtimes \Delta \overline{\boldsymbol{F}}^k_{e_r} . \boldsymbol{b}^{e^{k-1}{}^{-T}}_{e_r} . \overline{\boldsymbol{F}}^{k-1^{-T}}_{e_r} + \Delta \overline{\boldsymbol{F}}^k_{e_r} . \boldsymbol{b}^{e^{k-1}}_{e_r} . \overline{\boldsymbol{F}}^{k-1^{-T}}_{e_r} \boxdot \boldsymbol{I}$$

for an elastic step, and

$$\frac{\partial \boldsymbol{H}^k_{e_r}}{\partial \boldsymbol{u}^k_e} = \begin{bmatrix} -\frac{\partial \boldsymbol{b}^{e,tr}_{e_r}}{\partial \boldsymbol{u}^k_e} . \exp\left[-2\Delta t \boldsymbol{A}^k_{e_r}\right] & 0 & 0 \end{bmatrix}^T \tag{B.20}$$

for a plastic step. The nonzero submatrix $\partial \boldsymbol{H}^k / \partial \boldsymbol{u}^{k-1}$ in Eq. (B.16) has the same structure as in Eqn. (B.17) and (B.18), and the nonzero entries $\partial \boldsymbol{H}^k_{e_r} / \partial \boldsymbol{u}^{k-1}_e$ are

$$\frac{\partial \boldsymbol{H}_{e_r}^k}{\partial \boldsymbol{u}_e^{k-1}} = \left[-\frac{\partial \boldsymbol{b}_{e_r}^{e,tr}}{\partial \boldsymbol{u}_e^{k-1}} \quad 0 \quad 0 \right]^T$$

$$\frac{\partial \boldsymbol{b}_{e_r}^{e,tr}}{\partial \boldsymbol{u}_e^{k-1}} = \frac{\partial \boldsymbol{b}_{e_r}^{e,tr}}{\partial \overline{\boldsymbol{F}}_{e_r}^{k-1}} : \frac{\partial \overline{\boldsymbol{F}}_{e_r}^{k-1}}{\partial \boldsymbol{u}_e^{k-1}} \tag{B.21}$$

$$\frac{\partial \boldsymbol{b}_{e_r}^{e,tr}}{\partial \overline{\boldsymbol{F}}_{e_r}^{k-1}} = -\Delta \overline{\boldsymbol{F}}_{e_r}^k \boxtimes \Delta \overline{\boldsymbol{F}}_{e_r}^k . \boldsymbol{b}_{e_r}^{e^{k-1}{}^{-T}} . \overline{\boldsymbol{F}}_{e_r}^{k-1^{-T}} - \Delta \overline{\boldsymbol{F}}_{e_r}^k . \boldsymbol{b}_{e_r}^{e^{k-1}} . \overline{\boldsymbol{F}}_{e_r}^{k-1^{-T}} \boxdot \Delta \overline{\boldsymbol{F}}_{e_r}^k$$

for an elastic step and

$$\frac{\partial \boldsymbol{H}_{e_r}^k}{\partial \boldsymbol{u}_e^{k-1}} = \left[-\frac{\partial \boldsymbol{b}_{e_r}^{e,tr}}{\partial \boldsymbol{u}_e^{k-1}} . \exp\left[-2\Delta t \boldsymbol{A}_{e_r}^k \right] \quad 0 \quad 0 \right]^T \tag{B.22}$$

for a plastic step.

The derivatives $\partial \boldsymbol{H}^k / \partial \boldsymbol{c}^k$ and $\partial \boldsymbol{H}^k / \partial \boldsymbol{c}^{k-1}$, have the block diagonal matrix form

$$\frac{\partial \boldsymbol{H}^k}{\partial \boldsymbol{c}^k} = \begin{bmatrix} \frac{\partial \boldsymbol{H}_1^k}{\partial \boldsymbol{c}_1^k} & \boldsymbol{0} & \cdots & \boldsymbol{0} \\ \boldsymbol{0} & \frac{\partial \boldsymbol{H}_2^k}{\partial \boldsymbol{c}_2^k} & \cdots & \boldsymbol{0} \\ \vdots & \vdots & \ddots & \vdots \\ \boldsymbol{0} & \boldsymbol{0} & \cdots & \frac{\partial \boldsymbol{H}_{n_{ele}}^k}{\partial \boldsymbol{c}_{n_{ele}}^k} \end{bmatrix}, \frac{\partial \boldsymbol{H}^k}{\partial \boldsymbol{c}^{k-1}} = \begin{bmatrix} \frac{\partial \boldsymbol{H}_1^k}{\partial \boldsymbol{c}_1^{k-1}} & \boldsymbol{0} & \cdots & \boldsymbol{0} \\ \boldsymbol{0} & \frac{\partial \boldsymbol{H}_2^k}{\partial \boldsymbol{c}_2^{k-1}} & \cdots & \boldsymbol{0} \\ \vdots & \vdots & \ddots & \vdots \\ \boldsymbol{0} & \boldsymbol{0} & \cdots & \frac{\partial \boldsymbol{H}_{n_{ele}}^k}{\partial \boldsymbol{c}_{n_{ele}}^{k-1}} \end{bmatrix} \tag{B.23}$$

due to the fact that $\boldsymbol{c}_e^k$ and $\boldsymbol{c}_j^k$ are independent of each other and that $\boldsymbol{H}_e^k$ and $\boldsymbol{H}_j^k$ are uncoupled for $j \neq e$. The submatrices $\partial \boldsymbol{H}_e^k / \partial \boldsymbol{c}_e^k$ have this structure for the same reasons, i.e.

$$\frac{\partial \boldsymbol{H}_e^k}{\partial \boldsymbol{c}_e^k} = \begin{bmatrix} \frac{\partial \boldsymbol{H}_{e_1}^k}{\partial \boldsymbol{c}_{e_1}^k} & \boldsymbol{0} & \boldsymbol{0} & \boldsymbol{0} \\ \boldsymbol{0} & \frac{\partial \boldsymbol{H}_{e_2}^k}{\partial \boldsymbol{c}_{e_2}^k} & \boldsymbol{0} & \boldsymbol{0} \\ \boldsymbol{0} & \boldsymbol{0} & \frac{\partial \boldsymbol{H}_{e_3}^k}{\partial \boldsymbol{c}_{e_3}^k} & \boldsymbol{0} \\ \boldsymbol{0} & \boldsymbol{0} & \boldsymbol{0} & \frac{\partial \boldsymbol{H}_{e_4}^k}{\partial \boldsymbol{c}_{e_4}^k} \end{bmatrix}, \frac{\partial \boldsymbol{H}_e^k}{\partial \boldsymbol{c}_e^{k-1}} = \begin{bmatrix} \frac{\partial \boldsymbol{H}_{e_1}^k}{\partial \boldsymbol{c}_{e_1}^{k-1}} & \boldsymbol{0} & \boldsymbol{0} & \boldsymbol{0} \\ \boldsymbol{0} & \frac{\partial \boldsymbol{H}_{e_2}^k}{\partial \boldsymbol{c}_{e_2}^{k-1}} & \boldsymbol{0} & \boldsymbol{0} \\ \boldsymbol{0} & \boldsymbol{0} & \frac{\partial \boldsymbol{H}_{e_3}^k}{\partial \boldsymbol{c}_{e_3}^{k-1}} & \boldsymbol{0} \\ \boldsymbol{0} & \boldsymbol{0} & \boldsymbol{0} & \frac{\partial \boldsymbol{H}_{e_4}^k}{\partial \boldsymbol{c}_{e_4}^{k-1}} \end{bmatrix} \tag{B.24}$$

The nonzero entries $\partial \boldsymbol{H}_{e_r}^k / \partial \boldsymbol{c}_{e_r}^k$ are

$$\frac{\partial \boldsymbol{H}_{e_r}^k}{\partial \boldsymbol{c}_{e_r}^k} = \begin{bmatrix} \mathbb{I}_4^s & \boldsymbol{0} & \boldsymbol{0} \\ \boldsymbol{0} & 1 & 0 \\ \boldsymbol{0} & 0 & 1 \end{bmatrix} \tag{B.25}$$

for an elastic step, and

$$\frac{\partial \boldsymbol{H}_{e_r}^k}{\partial \boldsymbol{c}_{e_r}^k} = \begin{bmatrix} \mathbb{I}_4^s - \boldsymbol{b}_{e_r}^{e,tr} . \frac{\partial \exp\left[-2\Delta t \boldsymbol{A}_{e_r}^k \right]}{\partial \boldsymbol{b}_{e_r}^{e^k}} & \boldsymbol{0} & -\boldsymbol{b}_{e_r}^{e,tr} . \frac{\partial \exp\left[-2\Delta t \boldsymbol{A}_{e_r}^k \right]}{\Delta \gamma_{e_r}^k} \\ 0 & 1 & -1 \\ \sqrt{\frac{3}{2}} \left(\frac{\Delta t}{\mu \Delta \gamma_{e_r}^k + \Delta t} \right)^{\vartheta} \boldsymbol{n}_{e_r}^k : \frac{\partial \boldsymbol{\tau}_{e_r}^{VP^k}}{\partial \boldsymbol{b}_{e_r}^{e^k}} & -\frac{\partial \zeta}{\partial \alpha}\Big|_{\alpha = \alpha_{e_r}^k} & -c_0 \end{bmatrix} \tag{B.26}$$

$$c_0 = \sqrt{\frac{3}{2}} \left(\frac{\Delta t}{\mu \Delta \gamma_{e_r}^k + \Delta t} \right)^{\vartheta} \frac{\vartheta \mu \boldsymbol{s}_{e_r}^{VP^k}}{\mu \Delta \gamma_{e_r}^k + \Delta t}$$

for a plastic step. Again, the derivatives of the term $\exp[-2\Delta t\boldsymbol{A}^k_{e_r}]$ are computed in the principal space as

$$\frac{\partial \exp\left[-2\Delta\gamma\sqrt{\frac{3}{2}}n_a\right]}{\partial b^e_b} = -2\Delta\gamma\sqrt{\frac{3}{2}}\exp\left[-2\Delta\gamma\sqrt{\frac{3}{2}}n_a\right]\frac{\partial n_a}{\partial\tau_c}\left(\chi_S\frac{\partial\tau_c}{\partial b^e_b}\right), a,b,c=1,2,3$$
$$\frac{\partial \exp\left[-2\Delta\gamma\sqrt{\frac{3}{2}}n_a\right]}{\partial\Delta\gamma} = -2\sqrt{\frac{3}{2}}\exp\left[-2\Delta\gamma\sqrt{\frac{3}{2}}n_a\right]n_a \tag{B.27}$$

Finally, the nonzero entries of the derivative matrix $\partial\boldsymbol{H}^k/\partial\boldsymbol{c}^{k-1}$ are

$$\frac{\partial\boldsymbol{H}^k_{e_r}}{\partial\boldsymbol{c}^{k-1}_{e_r}} = \begin{bmatrix} -\frac{\partial\boldsymbol{b}^{e,tr}_{e_r}}{\partial\boldsymbol{b}^{e^{k-1}}_{e_r}} & \boldsymbol{0} & \boldsymbol{0} \\ \boldsymbol{0} & -1 & 0 \\ \boldsymbol{0} & 0 & 0 \end{bmatrix} \tag{B.28}$$
$$\frac{\partial\boldsymbol{b}^{e,tr}_{e_r}}{\partial\boldsymbol{b}^{e^{k-1}}_{e_r}} = \frac{1}{2}\left(\Delta\overline{\boldsymbol{F}}^k_{e_r}\boxtimes\Delta\overline{\boldsymbol{F}}^k_{e_r} + \Delta\overline{\boldsymbol{F}}^k_{e_r}\boxdot\Delta\overline{\boldsymbol{F}}^k_{e_r}\right)$$

for an elastic step and

$$\frac{\partial\boldsymbol{H}^k_{e_r}}{\partial\boldsymbol{c}^{k-1}_{e_r}} = \begin{bmatrix} -\frac{\partial\boldsymbol{b}^{e,tr}_{e_r}}{\partial\boldsymbol{b}^{e^{k-1}}_{e_r}}.\exp\left[-2\Delta t\boldsymbol{A}^k_{e_r}\right] & 0 & 0 \\ 0 & -1 & 0 \\ 0 & 0 & 0 \end{bmatrix} \tag{B.29}$$

where

$$\frac{\partial b^{e,tr}_{ip}\exp\left[-2\Delta tA_{pj}\right]}{\partial b^{e,k-1}_{kl}} = \frac{\partial b^{e,tr}_{ip}}{\partial b^{e,k-1}_{kl}}\exp\left[-2\Delta tA_{pj}\right]$$

for a plastic step.

B.3: Derivatives of objective function

From Eq. (26) it can be seen that the nonzero derivatives of the plastic work objective function are $\partial W^P/\partial\boldsymbol{\rho}$ and $\partial W^P/\partial\boldsymbol{c}^k$, which are given as

$$\frac{\partial W^p}{\partial\boldsymbol{\rho}} = \begin{bmatrix} \frac{\partial W^p}{\partial\rho_1} & \frac{\partial W^p}{\partial\rho_2} & \cdots & \frac{\partial W^p}{\partial\rho_{n_{ele}}} \end{bmatrix}$$
$$\frac{\partial W^p}{\partial\rho_e} = \sum_{k=1}^{n}\left(\sum_{r=1}^{n_{ipt}}\left(\frac{\partial\chi_A}{\partial\rho_e}w_r\sqrt{\frac{3}{2}}\Delta\gamma^k_{e_r}\boldsymbol{\tau}^{VP^k}_{e_r}:\boldsymbol{n}^k_{e_r} + \chi_A w_r\sqrt{\frac{3}{2}}\Delta\gamma^k_{e_r}\frac{\partial\boldsymbol{\tau}^{VP^k}_{e_r}}{\partial\rho_e}:\boldsymbol{n}^k_{e_r}\right)\right) \tag{B.30}$$
$$\frac{\partial\boldsymbol{\tau}^{VP^k}_{e_r}}{\partial\rho_e} = \frac{\partial\chi_S}{\partial\rho_e}\left(2\frac{\partial\psi_{VP}}{\partial\boldsymbol{b}^e}.\boldsymbol{b}^e\right)$$

and

$$\frac{\partial W^p}{\partial\boldsymbol{c}^k} = \begin{bmatrix} \frac{\partial W^p}{\partial\boldsymbol{c}^k_1} & \frac{\partial W^p}{\partial\boldsymbol{c}^k_2} & \cdots & \frac{\partial W^p}{\partial\boldsymbol{c}^k_{n_{ele}}} \end{bmatrix}$$
$$\frac{\partial W^p}{\partial\boldsymbol{c}^k_e} = \begin{bmatrix} \frac{\partial W^p}{\partial\boldsymbol{c}^k_{e_1}} & \frac{\partial W^p}{\partial\boldsymbol{c}^k_{e_2}} & \frac{\partial W^p}{\partial\boldsymbol{c}^k_{e_3}} & \frac{\partial W^p}{\partial\boldsymbol{c}^k_{e_4}} \end{bmatrix} \tag{B.31}$$
$$\frac{\partial W^p}{\partial\boldsymbol{c}^k_{e_r}} = \chi_A w_r\sqrt{\frac{3}{2}}\begin{bmatrix} \Delta\gamma^k_{e_r}\left(\frac{\partial\boldsymbol{\tau}^{VP^k}_{e_r}}{\partial\boldsymbol{b}^{e^k}_{e_r}}:\boldsymbol{n}^k_{e_r} + \boldsymbol{\tau}^{VP^k}_{e_r}:\frac{\partial\boldsymbol{n}^k_{e_r}}{\partial\boldsymbol{b}^{e^k}_{e_r}}\right) & 0 & \boldsymbol{\tau}^{VP^k}_{e_r}:\boldsymbol{n}^k_{e_r} \end{bmatrix}^T$$

where the derivatives $\partial \boldsymbol{\tau}_{e_r}^{VP^k} / \partial \boldsymbol{b}_{e_r}^{e^k}$ and $\partial \boldsymbol{n}_{e_r}^{k} / \partial \boldsymbol{b}_{e_r}^{e^k}$ are evaluated in principal space and then transformed to physical space.

References

[1] M.P. Bendsøe, N. Kikuchi, Generating optimal topologies in structural design using a homogenization method, Comput. Methods Appl. Mech. Eng. 71 (1988) 197–224, https://doi.org/10.1016/0045-7825(88)90086-2.

[2] H.A. Eschenauer, N. Olhoff, Topology optimization of continuum structures: a review*, Appl. Mech. Rev. 54 (2001) 331–390, https://doi.org/10.1115/1.1388075.

[3] O. Sigmund, K. Maute, Topology optimization approaches, Struct. Multidiscip. Optim. 48 (2013) 1031–1055, https://doi.org/10.1007/s00158-013-0978-6.

[4] J.D. Deaton, R.V. Grandhi, A survey of structural and multidisciplinary continuum topology optimization: post 2000, Struct. Multidiscip. Optim. 49 (2014) 1–38, https://doi.org/10.1007/s00158-013-0956-z.

[5] M.P. Bendsøe, O. Sigmund, Topology Optimization: Theory, Methods and Applications, second ed. ed., Springer, Berlin, 2003.

[6] U. Schramm, M. Zhou, Recent Developments in the Commercial Implementation of Topology Optimization, Springer Netherlands, Dordrecht, 2006, pp. 239–248.

[7] D.W. Rosen, A review of synthesis methods for additive manufacturing, Virtual Phys. Prototyp. 11 (2016) 305–317, https://doi.org/10.1080/17452759.2016.1240208.

[8] G. Lu, T. Yu, Energy Absorption of Structures and Materials, Taylor & Francis, Abington Cambridge, England, 2003.

[9] C.C. Swan, I. Kosaka, Homogenization-based analysis and design of composites, Comput. Struct. 64 (1997) 603–621, https://doi.org/10.1016/S0045-7949(96)00158-7.

[10] C.C. Swan, I. Kosaka, Voigt-Reuss topology optimization for structures with nonlinear material behaviors, Int. J. Numer. Methods Eng. 40 (1997) 3785–3814, https://doi.org/10.1002/(SICI)1097-0207(19971030)40:20<3785::AID-NME240>3.0.CO;2-V.

[11] K. Maute, S. Schwarz, E. Ramm, Adaptive topology optimization of elastoplastic structures, Struct. Optim. 15 (1998) 81–91, https://doi.org/10.1007/BF01278493.

[12] S. Schwarz, K. Maute, E. Ramm, Topology and shape optimization for elastoplastic structural response, Comput. Methods Appl. Mech. Eng. 190 (2001) 2135–2155, https://doi.org/10.1016/S0045-7825(00)00227-9.

[13] M. Bogomolny, O. Amir, Conceptual design of reinforced concrete structures using topology optimization with elastoplastic material modeling, Int. J. Numer. Methods Eng. 90 (2012) 1578–1597.

[14] G. Zhang, L. Li, K. Khandelwal, Topology optimization of structures with anisotropic plastic materials using enhanced assumed strain elements, Struct. Multidiscip. Optim. (2016) 1–24, https://doi.org/10.1007/s00158-016-1612-1.

[15] L. Li, G. Zhang, K. Khandelwal, Design of energy dissipating elastoplastic structures under cyclic loads using topology optimization, Struct. Multidiscip. Optim. 56 (2017) 391–412, https://doi.org/10.1007/s00158-017-1671-y.

[16] R. Alberdi, K. Khandelwal, Topology optimization of pressure dependent elastoplastic energy absorbing structures with material damage constraints, Finite Elem. Anal. Des. 133 (2017) 42–61. https://doi.org/10.1016/j.finel.2017.05.004.

[17] L. Li, G. Zhang, K. Khandelwal, Topology optimization of energy absorbing structures with maximum damage constraint, Int. J. Numer. Methods Eng. (2017), https://doi.org/10.1002/nme.5531.

[18] L. Li, G. Zhang, K. Khandelwal, Failure resistant topology optimization of structures using nonlocal elastoplastic-damage model, Struct. Multidiscip. Optim. 58 (2018) 1589–1618, https://doi.org/10.1007/s00158-018-1984-5.

[19] M. Wallin, V. Jönsson, E. Wingren, Topology optimization based on finite strain plasticity, Struct. Multidiscip. Optim. (2016) 1–11, https://doi.org/10.1007/s00158-016-1435-0.

[20] R. Behrou, J.K. Guest, Topology optimization for transient response of structures subjected to dynamic loads, in: 18th AIAA/ISSMO Multidisciplinary Analysis and Optimization Conference, American Institute of Aeronautics and Astronautics, 2017.

[21] K.-S. Yun, S.-K. Youn, Multi-material topology optimization of viscoelastically damped structures under time-dependent loading, Finite Elem. Anal. Des. 123 (2017) 9–18, https://doi.org/10.1016/j.finel.2016.09.006.

[22] K.-S. Yun, S.-K. Youn, Topology optimization of viscoelastic damping layers for attenuating transient response of shell structures, Finite Elem. Anal. Des. 141 (2018) 154–165, https://doi.org/10.1016/j.finel.2017.12.003.

[23] P. Nakshatrala, D. Tortorelli, Topology optimization for effective energy propagation in rate-independent elastoplastic material systems, Comput. Methods Appl. Mech. Eng. 295 (2015) 305–326, https://doi.org/10.1016/j.cma.2015.05.004.

[24] N. Ivarsson, M. Wallin, D. Tortorelli, Topology optimization of finite strain viscoplastic systems under transient loads, Int. J. Numer. Methods Eng. 114 (2018) 1351–1367, https://doi.org/10.1002/nme.5789.

[25] E.A. de Souza Neto, D. Peric, M. Dutko, D.R.J. Owen, Design of simple low order finite elements for large strain analysis of nearly incompressible solids, Int. J. Solids Struct. 33 (1996) 3277–3296. https://doi.org/10.1016/0020-7683(95)00259-6.

[26] H.M. Hilber, T.J.R. Hughes, R.L. Taylor, Improved numerical dissipation for time integration algorithms in structural dynamics, Earthq. Eng. Struct. Dyn. 5 (1977) 283–292, https://doi.org/10.1002/eqe.4290050306.

[27] R. Alberdi, G. Zhang, L. Li, K. Khandelwal, A unified framework for nonlinear path-dependent sensitivity analysis in topology optimization, Int. J. Numer. Methods Eng. 115 (2018) 1–201856, https://doi.org/10.1002/nme.5794.

[28] E.A. de Souza Neto, D. Peric, D.R.J. Owen, Computational Methods for Plasticity: Theory and Applications, John Wiley & Sons Ltd., West Sussex, England, 2011.

[29] G.A. Holzapfel, Nonlinear Solid Mechanics: A Continuum Approach for Engineering, Wiley, 2000.

[30] D. Perić, On a class of constitutive equations in viscoplasticity: formulation and computational issues, Int. J. Numer. Methods Eng. 36 (1993) 1365–1393, https://doi.org/10.1002/nme.1620360807.

[31] D. Peric, W. Dettmer, A computational model for generalized inelastic materials at finite strains combining elastic, viscoelastic and plastic material behaviour, Eng. Comput. 20 (2003) 768–787, https://doi.org/10.1108/02644400310488862.

[32] F. Armero, Elastoplastic and viscoplastic deformations in solids and structures, in: E. Stein, R. De Borst, T.J.R. Hughes (Eds.), Encyclopedia of Computational Mechanics, second ed., John Wiley & Sons, Ltd., 2017, pp. 227–266.

[33] T.E. Bruns, D.A. Tortorelli, Topology optimization of non-linear elastic structures and compliant mechanisms, Comput. Methods Appl. Mech. Eng. 190 (2001) 3443–3459. https://doi.org/10.1016/S0045-7825(00)00278-4.

[34] B. Bourdin, Filters in topology optimization, Int. J. Numer. Methods Eng. 50 (2001) 2143–2158, https://doi.org/10.1002/nme.116.

[35] L. Li, K. Khandelwal, Volume preserving projection filters and continuation methods in topology optimization, Eng. Struct. 85 (2015) 144–161, https://doi.org/10.1016/j.engstruct.2014.10.052.

[36] P. Christensen, A. Klarbring, An Introduction to Structural Optimization, Springer, 2009.

[37] P.M. Bendsøe, O. Sigmund, Material Interpolation Schemes in Topology Optimization vol. 69, Archive of Applied Mechanics, 1999, pp. 635–654, https://doi.org/10.1007/s004190050248.

[38] J. Kato, H. Hoshiba, S. Takase, K. Terada, T. Kyoya, Analytical sensitivity in topology optimization for elastoplastic composites, Struct. Multidiscip. Optim. 52 (2015) 507–526, https://doi.org/10.1007/s00158-015-1246-8.

[39] W. Voigt, Ueber die Beziehung zwischen den beiden Elasticitatsconstanten isotroper Korper, Ann. Phys. 274 (1889) 573–587, https://doi.org/10.1002/andp.18892741206.

[40] A. Reuss, Berechnung der fliessgrenze von mischkristallen auf grund der plastizitatsbedingung Fur einkristalle, ZAMM J. App. Math. Mechanics/Zeitschrift fur Angewandte Mathematik und Mechanik 9 (1929) 49–58.

[41] C.C. Swan, J.S. Arora, Topology design of material layout in structured composites of high stiffness and strength, Struct. Optim. 13 (1997) 45–59, https://doi.org/10.1007/bf01198375.

[42] G.I. Taylor, Plastic strain in metals, J. Inst. Met. 62 (1938) 307–324.

[43] M.A. Crisfield, in: Non-linear Finite Element Analysis of Solids and Structures, John Wiley & Sons Ltd, West Sussex, England, 1991.

[44] K. Svanberg, The method of moving asymptotes—a new method for structural optimization, Int. J. Numer. Methods Eng. 24 (1987) 359–373, https://doi.org/10.1002/nme.1620240207.

[45] G. Zhang, R. Alberdi, K. Khandelwal, Topology optimization with incompressible materials under small and finite deformations using mixed u/p elements, Int. J. Numer. Methods Eng. 115 (2018) 1015–1052, https://doi.org/10.1002/nme.5834.